

## Chapter 9

# Corrosion by Carbon

### 9.1 INTRODUCTION

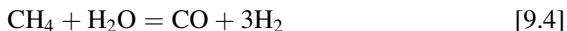
The combustion of fossil fuels (coal, oil, natural gas) provides the basis for a major part of the world's energy generation. This includes burning fuel to raise steam for electric power generation and combustion of liquid fuels for transportation. The combustion reactions



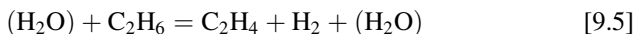
are often carried out using excess air, so that the exhaust gases contain free molecular oxygen plus  $CO_2$  and  $H_2O$ . Despite the use of excess air or oxygen, locally reducing conditions can develop and persist in large-scale combustion units. Such conditions can lead to carbon attack, as is discussed shortly. The behaviour of  $CO_2$  as a corrodent acting alone, ie, in the absence of free oxygen or reducing gases, is dealt with in Chapter 10.

There is a continuing drive to improve the efficiency of combustion processes. Not only are temperatures being raised to achieve higher efficiencies (Eq. [1.6]), but alternative or modified technologies are being developed to reduce emissions of the greenhouse gas,  $CO_2$ . The capture and sequestration of  $CO_2$  is made more feasible by using pure oxygen rather than air as oxidant, thereby eliminating nitrogen from the combustion gas. Because combustion in pure oxygen leads to excessively high flame temperatures, some of the exhaust  $CO_2$  is recirculated as a diluent for the input oxygen. As a result, the combustion zone gases contain very high concentrations of  $CO_2$  and  $H_2O$ . Little is known of the behaviour of heat-resisting alloys in such environments. However, given earlier observations (Section 4.5) of carbon deposition within oxide scales exposed to  $CO_2/CO$  atmospheres, there seems to be a need for research in this area.

A number of other high-temperature processes are conducted under reducing conditions so as to produce hydrogen or CO, rather than their oxidation products. Steam reforming of natural gas



is widely used to produce hydrogen. This process is carried out at temperatures of around 800–900°C by passing the gases through catalyst beds in alloy tubes heated from the exterior. Somewhat similar tubular reactors are used in the pyrolysis or ‘steam cracking’ process for making ethylene or propylene, eg,



In this case the steam is added as a diluent in order to reduce the amount of solid carbon produced by gas-phase pyrolysis.

Feedstock materials, or hydrocarbons, have risen in price at times, and the need for improved process efficiencies has led to higher operating temperatures. Simultaneously, tube wall thicknesses have been reduced to improve heat-transfer efficiency. Thus process engineering changes have led to higher tube metal temperatures and reduced load-bearing sections. These increased demands on material properties have been met by a series of advances in alloy design. The tubes are centrifugally cast, austenitic chromia-formers. Their compositions (Table 9.1) have evolved from the old HK 40 grade (Fe-25Cr-20Ni), through the HP grades (Fe-25Cr-35Ni) to high-nickel alloys containing 45 or even 60% Ni. The increased alloy levels have provided significant improvements in creep properties, but the alloys are still subject to corrosion by carbon.

The process of coal gasification is of potential importance in achieving high-efficiency electric power generation. Steam is contacted with coal at high temperatures, producing synthesis gas



Although coal gasification has been employed for a long time, its use on the scale and at the intensity required to support gas turbine-driven power generation is relatively new. The selection of materials for handling and processing the hot carbonaceous gases produced from coal will depend on the gasification technologies chosen, and the coal impurity levels involved. However, the carbon corrosion mechanisms can be expected to be related to those observed in steam reforming and steam cracking plants.

Under combustion conditions, the oxygen potential is usually high enough to guarantee oxide scale formation. The questions of interest then concern interaction of CO<sub>2</sub> with the oxide. In contrast, synthesis gas and other carbonaceous gases handled in the chemical and petrochemical industries are characterised by high carbon activity,  $a_{\text{C}}$ , values and low oxygen potentials. Typically these gases are oxidising to chromium and aluminium, but not to iron or nickel. The questions of interest therefore concern the ability of Cr<sub>2</sub>O<sub>3</sub> and Al<sub>2</sub>O<sub>3</sub> scales to exclude carbon from the alloy, and the consequences of

**TABLE 9.1 Heat-Resisting Alloy Compositions (wt.%)**

	C	Si	Mn	Ni	Cr	Nb	Al	Other
<b>Cast Alloys</b>								
HK40	0.4	1.3	0.6	21	25			
HP	0.4	1.8	1.1	35	25	0.8		0.1Zr, 0.2Ti
HP Mod Nb	0.44	1.5	1.5	35	25	1.5		
H101	0.09	2.2	1.1	36	26	1		
30Cr Micro	0.53	2.1	0.3	29	30	1		0.11Ce
35/45	0.46	2.1	1.2	45	35	1		
45Pa	0.45	1	0.4	45	19	0.4	2	3Mo 0.3-1.5Hf
45HT	0.44	1	0.5	45	30	0.5	0.5	0-0.8Hf
60HT(a)	0.42	0.1	0.1	60	25	1	2.4	0.06Y
60HT(b)	0.40	0.0	0.2	61	25		3.6	0.05Y
60HT(c)	0.43	0.1	0.1	59	25	1	4.8	0.06Y
<b>Wrought Alloys</b>								
304L	0.03	1	2	8	18			
310S	0.08	1.5	2	19	24			

*Continued*

**TABLE 9.1 Heat-Resisting Alloy Compositions (wt.%)—cont'd**

	C	Si	Mn	Ni	Cr	Nb	Al	Other
800	0.1	0.4	0.7	32	20		0.3	0.4Ti
601	0.03	0.3	0.2	60	22		1.4	0.4Ti
625	0.02	0.1	0.1	60	22		0.4	9Mo, 3.4(Nb + Ta), 0.2Ti
690	0.02	0.1	0.1	61	27		0.2	0.2Ti
693	0.01	0.1	0.2	61	29	0.45	3.2	0.4Ti
602CA	0.2	0.05	0.1	63	20		2.3	0.1Ti, 0.09Y, 0.08 Zr

oxide scale failure when carbonaceous gas species contact the metal surface. We consider first the simple case where the oxygen potential is so low that no oxide forms, and corrosion by carbon alone results.

Carbon is unique among the common oxidants in that it is stable as a solid over a wide temperature range if the gas is sufficiently reducing. For this reason, the thermodynamic reference state is chosen as pure, solid graphite, for which  $a_C = 1$ . If the carbon activity is less than one, but large enough to stabilise a metal carbide, the reaction is described as carburisation. Such reactions are rapid and destructive. However, if the gas is supersaturated with respect to carbon ( $a_C > 1$ ), an even greater threat emerges. If the gas can be brought to equilibrium, carbon is released from the gas phase and deposits on solid surfaces in a process described as coking. Frequently, however, the gas remains supersaturated. In this case, catalysis of carbon deposition by the metal can lead to its disruption and fragmentation in an extremely rapid corrosion process known as metal dusting. Dusting mechanisms are different for ferritic and austenitic alloys, and they will be discussed separately. Alloy design strategies for slowing carburisation and metal dusting are shown to be of limited value. However, alloying to achieve protective oxide formation can delay carbon access to the metal. This approach is discussed together with other surface treatments in [Section 9.8](#).

## 9.2 GASEOUS CARBON ACTIVITIES

The common gas-phase processes producing carbon are the synthesis gas reaction



the Boudouard reaction



and hydrocarbon cracking, eg,



Their standard free energies are listed in [Table 9.2](#). It is necessary to recognise that all three reactions are very slow as homogenous gas-phase processes. They will not reach equilibrium in a typical laboratory reactor, unless catalysed. Although many materials of practical interest – iron, nickel, cobalt and their alloys – are catalytically active to these reactions, their oxide scales are inert.

As seen in [Table 9.2](#) and [Fig. 9.1](#), temperature effects are very different for these carbon-producing reactions. Thus methane, and hydrocarbons in general, can produce significant carbon activities only at high temperatures. On the other hand, the synthesis gas and Boudouard reactions produce increasing carbon activities as the temperature is lowered.

**TABLE 9.2 Gas-Phase Equilibria Relevant to Carburising [10]**

Reaction	$\Delta G_f^\circ = A + BT \text{ (J mol}^{-1}\text{)}$	
	A	B
$\text{CO} + \text{H}_2 = \text{H}_2\text{O} + \text{C}$	-134,515	142.37
$2\text{CO} = \text{CO}_2 + \text{C}$	-170,700	174.5
$\text{CH}_4 = 2\text{H}_2 + \text{C}$	+87,399	-108.74

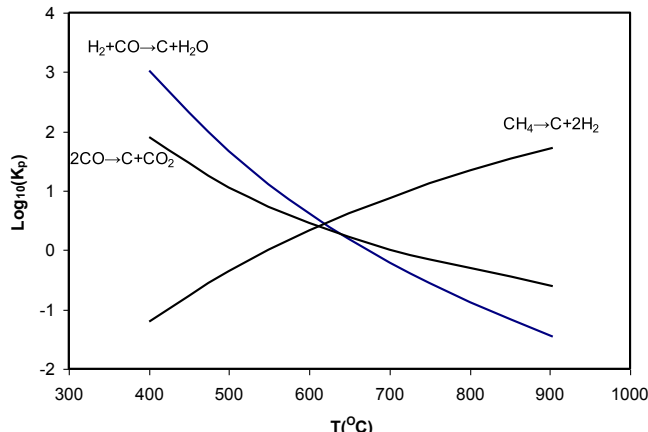
It is because these gases are difficult to equilibrate that they can become supersaturated with respect to carbon, ie,  $a_{\text{C}} > 1$ . An example is synthesis gas produced in a steam reforming unit, which will normally have  $a_{\text{C}} < 0.5$ . As the gas is cooled from reaction temperature, however, the rate of reaction Eq. [9.7] is so slow that the gas fails to adjust its composition by depositing carbon. The gas-phase carbon activity calculated from

$$a_{\text{C}}(7) = \frac{K_7 p_{\text{H}_2} p_{\text{CO}}}{p_{\text{H}_2\text{O}}} \quad [9.10]$$

can then be much greater than unity. It is recognised that the same gas also produces carbon via Eq. [9.8], and one can calculate

$$a_{\text{C}}(8) = \frac{K_8 p_{\text{CO}}^2}{p_{\text{CO}_2}} \quad [9.11]$$

In general,  $a_{\text{C}}(7) \neq a_{\text{C}}(8)$ , because the gas is not at equilibrium. In this situation, it is appropriate to consider the Eqs [9.7–9.9] as separate, independent

**FIGURE 9.1** Equilibrium constants for gas-phase carbon-producing reactions.

processes, as is demonstrated in Sections 9.6 and 9.7. Nonetheless, because Eq. [9.7] is usually faster than Eq. [9.8], it is common to calculate  $a_C$  from Eq. [9.10].

The water vapour present in many gas mixtures is also capable of interaction with surface oxide scales, as is discussed in Chapter 11. Of course, these effects can be ignored in the reducing conditions characteristic of many carburisation and dusting reactions. However, they can be important in the situation where an oxide scale is relied upon for protection against carbon attack. Some of the interactions between  $\text{H}_2\text{O}(g)$  and carbon species are discussed in Chapters 4 and 11.

Carburisation experiments require  $a_C \leq 1$ . The use of  $\text{CH}_4/\text{H}_2$  gas mixtures to control carbon activity is inadvisable at temperatures below about  $1000^\circ\text{C}$ , because of the slow rate of Eq. [9.9] and the usually brief residence time in a laboratory reactor. It is preferable to use mixtures of  $\text{H}_2$  and  $\text{C}_3\text{H}_6$ , as the latter pyrolyses readily.

### 9.3 CARBURISATION

Carbides are much less stable than oxides, as seen from the examples in Table 9.3. Thermodynamic data for other carbides can be found in a review by Shatynski [1]. Of the common alloy base metals, nickel and cobalt do not form carbides under the conditions of interest. (Iron forms cementite,  $\text{Fe}_3\text{C}$ , at temperatures below  $763^\circ\text{C}$  only if  $a_C > 1$ .) Exposure of these metals to reducing carbonaceous gases therefore cannot cause scale formation but leads instead to dissolution of carbon at the metal surface and its diffusion inwards. If the metal surface is at equilibrium with the gas phase, the surface

**TABLE 9.3 Properties of Metal Carbides [1,10]**

Carbide	$\Delta G_f^\circ = A + BT (\text{J mol}^{-1})$		$V_{MC_y}^*/\text{cm}^3$	$\text{MP}/^\circ\text{C}$
	A	B		
$\text{Cr}_{23}\text{C}_6$	-411,200	-38.7	7.91	1580
$\text{Cr}_7\text{C}_3$	-174,509	-25.5	8.26	1665
$\text{Cr}_3\text{C}_2$	-84,353	-11.53	8.98	1895
NbC	-130,122	+1.67	13.47	3480
SiC	-113,386	+75.7	13.70	2700
$\text{Al}_4\text{C}_3$	-266,520	+96.2	15.24	$\sim 1400$
$\text{Fe}_3\text{C}$	29,037	-28.0	8.31	1650

\*Volume per mole of metal.

**TABLE 9.4** Carbon Dissolution in Metals

Metal	$\Delta\bar{H}_C/\text{kJ mole}^{-1}$	$\Delta\bar{S}_C^{\text{xs}}/\text{J mole}^{-1}\text{ K}^{-1}$	References
Ni	54	5	[3]
$\gamma$ -Fe	44.04	17.62	[2]

concentration of dissolved carbon  $N_C^{(\text{s})}$  (mole fraction), can be found from the relationship

$$N_C^{(\text{s})} = K a_C \quad [9.12]$$

Data for carbon dissolution in iron and nickel are summarised in [Table 9.4](#), where the carbon solubility in nickel is seen to be much lower than in  $\gamma$ -Fe. If inward carbon diffusion causes no phase change in the solvent metal, and if furthermore  $D_C$  is independent of composition, then the resulting carbon concentration profile is found by solving Fick's second law to obtain

$$\frac{N_C - N_C^{(\text{o})}}{N_C^{(\text{s})} - N_C^{(\text{o})}} = \operatorname{erfc}\left(\frac{x}{2\sqrt{D_C t}}\right) \quad [9.13]$$

Here  $N_C^{(\text{o})}$  represents the original carbon level in the metal prior to carburisation. The rate at which the carburisation zone widens is given approximately by

$$X_i^2 = 4D_C t \quad [9.14]$$

Using data for  $D_C$  [\[4,5\]](#) (see [Table D2](#)), it is found that carbon penetrates about 3 mm into each of  $\gamma$ -Fe and Ni in 24 h at 1000°C. It is concluded that not only are Fe-, Ni- and Co-base alloys susceptible to internal attack, but the process will be rapid. Such high rates of attack are usually averted by designing the alloy to develop a protective oxide scale.

The heat-resisting alloys used in contact with carbon-rich gases are usually chromia formers. As seen in [Table 9.3](#), chromium also forms reasonably stable carbides. It is commonly observed [\[6–8\]](#) that exposure of these alloys to gas compositions such that no chromia scale can form leads to internal chromium carbide precipitation rather than external scale formation. The conditions under which this reaction morphology develops are now examined using model Fe-Cr, Ni-Cr and Fe-Ni-Cr alloys, for which the necessary data are available.

## 9.4 INTERNAL CARBURISATION OF MODEL ALLOYS

### 9.4.1 Reaction Morphologies and Thermodynamics

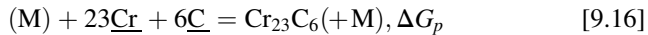
Chromium carbides are the expected reaction products, and their formation within the alloy is the outcome of competition between rival processes. Scale

formation is favoured by rapid diffusion of chromium from the alloy to its surface, whereas internal precipitation is favoured by rapid carbon ingress. Wagner's analysis [9] (Section 6.11) of this situation allows calculation of the minimum value of  $N_{\text{Cr}}^{(o)}$  at which scaling is favoured over internal precipitation

$$N_{\text{Cr}}^{(o)} = \left( g_{\text{CrC}_v} \frac{\pi}{2v} \frac{V_A}{V_{\text{CrC}_v}} \frac{N_C^{(s)} D_C}{D_{\text{Cr}}} \right)^{\frac{1}{2}} \quad [9.15]$$

Here  $g$  is the critical volume fraction necessary to form a continuous layer,  $V_A$  and  $V_{\text{CrC}_v}$  are the molar volumes of alloy and carbide,  $D_C$  and  $D_{\text{Cr}}$  are the diffusion coefficients in the alloy of the indicated solutes and  $v$  is the stoichiometric constant for the carbide  $\text{CrC}_v$ . Choosing Nimonic 75 (approximately Ni-20Cr) as a basis for calculation, we can specify  $V_A = 6.58 \text{ cm}^3 \text{ mole}^{-1}$ . Values for carbon permeability ( $N_C^{(s)} D_C$ ) and  $D_{\text{Cr}}$  listed in Table 9.5, together with  $V_{\text{CrC}_v}$  taken from Table 9.3 and the supposition  $g = 0.3$ , lead to estimates of  $N_{\text{Cr}}^{(o)} = 15, 20$  and  $37$  required to form scales of  $\text{Cr}_3\text{C}_2$ ,  $\text{Cr}_7\text{C}_3$  and  $\text{Cr}_{23}\text{C}_6$ , respectively, at  $1000^\circ\text{C}$ . Of course values of  $N > 1$  lack physical significance, and result from inaccuracies in the data. The conclusion is simply that Ni-Cr alloys are unlikely to form carbide scales exclusively, because the inward carbon flux is so high and the molar volumes of chromium carbides are small.

The conditions necessary for carbide precipitation are now examined more closely. In the case of  $\text{Cr}_{23}\text{C}_6$ , we can write



the free energy change for which can be calculated from data for carbide formation



and alloy component dissolution

**TABLE 9.5 Permeability Data for Carburisation**

Alloy	T/°C	$N_C^{(s)} D_C$	$D_{\text{Cr}}$
$\gamma$ -Fe	900	$4.3 \times 10^{-9}$	$4.4 \times 10^{-13}$
	1000	$1.4 \times 10^{-8}$	$3.7 \times 10^{-12}$
	1100	$5.5 \times 10^{-8}$	$2.3 \times 10^{-11}$
Ni	900	$7.9 \times 10^{-10}$	$8.0 \times 10^{-13}$
	1000	$3.6 \times 10^{-9}$	$7.2 \times 10^{-12}$
	1100	$1.4 \times 10^{-8}$	$4.7 \times 10^{-11}$

$$\text{Cr} = \underline{\text{Cr}}, \quad \Delta\bar{G}_{\text{Cr}} \quad [9.18]$$

$$\text{C} = \underline{\text{C}}, \quad \Delta\bar{G}_{\text{C}} \quad [9.19]$$

in the solvent metal, M. Thus

$$\Delta G_p = \Delta G_f^\circ - 23\Delta\bar{G}_{\text{Cr}} - 6\Delta\bar{G}_{\text{C}} \quad [9.20]$$

and we evaluate the carbide solubility product

$$N_{\text{Cr}}^{23} N_{\text{C}}^6 = K_{\text{sp}} = \exp[(\Delta G_f^\circ - 23\Delta\bar{H}_{\text{Cr}} - 6\Delta\bar{H}_{\text{C}})/RT] \quad [9.21]$$

with  $\bar{H}_i$  the partial molar heat of dissolution. A similar treatment for  $\text{Cr}_7\text{C}_3$  leads to the result

$$N_{\text{Cr}}^7 N_{\text{C}}^3 = K_{\text{sp}} = \exp[(\Delta G_f^\circ - 7\Delta\bar{H}_{\text{Cr}} - 6\Delta\bar{H}_{\text{C}})/RT] \quad [9.22]$$

Standard values (Table 9.3) for  $\Delta G_f^\circ$ , carbon solubility data for  $\gamma$ -Fe [2] and Ni [3] and activity coefficient data for Fe-Cr [10] and Ni-Cr [11] allow calculation of carbide solubility product values shown in Tables 9.6 and 9.7.

Carbon solute levels in  $\gamma$ -Fe and Ni in equilibrium with  $a_{\text{C}} = 1$  are also shown in the tables, along with the corresponding minimum chromium concentrations necessary to stabilise each carbide. Iron-base alloys are predicted on this basis to be more susceptible to internal carbide precipitation. This prediction is tested by comparing the calculated minimum  $N_{\text{Cr}}$  values required for carbide precipitation with the experimental results for 1000°C summarised in Table 9.8. The appearance of the carbide precipitation zones in Fe-Cr alloys is illustrated in Fig. 9.2. As predicted, Fe-Cr alloys of high chromium content formed both carbides whereas Ni-Cr formed only  $\text{Cr}_7\text{C}_3$ . Furthermore, the prediction that no carbide should form in Ni-Cr with  $N_{\text{Cr}}^{(0)} < 0.13$  is borne out.

The success of this simple thermodynamic treatment indicates that local equilibrium is attained, and a steady-state diffusion description should therefore be applicable. However, whilst the assumption that the chromium carbides are pure phases – the basis for Eqs [9.21] and [9.22] – is reasonable for the

**TABLE 9.6** Calculated Chromium Carbide Precipitation in Fe-Cr Alloys at  $a_{\text{C}} = 1$

Alloy	900°C	1000°C	1100°C
$N_{\text{C}}^{(\text{s})}(\gamma\text{-Fe})$	0.057	0.066	0.098
$K_{\text{sp}}(\text{Cr}_{23}\text{C}_6)$	$1 \times 10^{-29}$	$3.6 \times 10^{-27}$	$2.6 \times 10^{-24}$
$N_{\text{Cr}}(\text{min})$	0.12	0.14	0.17
$K_{\text{sp}}(\text{Cr}_7\text{C}_3)$	$3 \times 10^{-16}$	$3.8 \times 10^{-15}$	$3.4 \times 10^{-14}$
$N_{\text{Cr}}(\text{min})$	0.02	0.03	0.03

**TABLE 9.7** Calculated Chromium Carbide Precipitation in Ni-Cr Alloys at  $a_C = 1$ 

Alloy	900°C	1000°C	1100°C
$N_{\text{Cr}}^{(s)}$	0.007	0.011	0.016
$K_{sp}(\text{Cr}_{23}\text{C}_6)$	$9.9 \times 10^{-26}$	$8.4 \times 10^{-24}$	$3.7 \times 10^{-22}$
$N_{\text{Cr}}(\text{min})$	0.29	0.32	0.34
$K_{sp}(\text{Cr}_7\text{C}_3)$	$9.8 \times 10^{-14}$	$9.4 \times 10^{-13}$	$6.5 \times 10^{-12}$
$N_{\text{Cr}}(\text{min})$	0.10	0.13	0.17

**TABLE 9.8** Internal Carbides Found in Ni-Cr [12,13] and Fe-Cr [14] at 1000°C and Ambient  $a_C = 1$ 

Alloy	$N_{\text{Cr}}^{(o)}$	Surface Carbides	Internal Carbides	References
Ni-Cr	0.11	None	None	[12]
	0.22	$\text{Cr}_3\text{C}_2$	$\text{Cr}_7\text{C}_3$	[12]
	0.33		$\text{Cr}_7\text{C}_3$	[13]
Fe-Cr	0.05	$\text{Fe}_3\text{C}$	$\text{M}_7\text{C}_3^{\text{a}}$	[14]
	0.08	$\text{Fe}_3\text{C}$	$\text{M}_7\text{C}_3$	[14]
	0.11	$\text{Fe}_3\text{C}$	$\text{M}_7\text{C}_3$	[14]
	0.18	$\text{M}_7\text{C}_3^{\text{a}}$	$\text{M}_7\text{C}_3 + \text{M}_{23}\text{C}_6$	[14]
	0.26	$\text{M}_7\text{C}_3$	$\text{M}_7\text{C}_3 + \text{M}_{23}\text{C}_6$	[14]

<sup>a</sup>M: chromium-rich ( $\text{Cr} + \text{Fe}$ ).

Ni-Cr-C system, it is a poor approximation for Fe-Cr-C. As seen in the phase diagram of Fig. 9.3, iron solubilities in the carbides are high and cannot be neglected. It is possible to calculate  $K_{sp}$  values for the mixed carbides  $(\text{Cr}, \text{Fe})_{23}\text{C}_6$  and  $(\text{Cr}, \text{Fe})_7\text{C}_3$ , but a simpler approach is to construct diffusion paths representing the locus of compositions along lines through the reaction zone. Because  $D_{\text{C}} \gg D_{\text{Cr}}$ , these paths are constructed on the basis that only carbon diffuses and hence the  $N_{\text{Cr}}/N_{\text{Fe}}$  ratio remains unchanged within the reaction zone.

The diffusion path in Fig. 9.3 for  $N_{\text{Cr}}^{(o)} = 0.08$  is seen to cross the  $\gamma + \text{M}_7\text{C}_3$  two-phase region, corresponding to internal precipitation of this carbide, before entering the single-phase  $\text{M}_3\text{C}$  zone, in agreement with experimental observation (Table 9.7). An alloy with  $N_{\text{Cr}}^{(o)} = 0.18$  is seen to develop a carbon

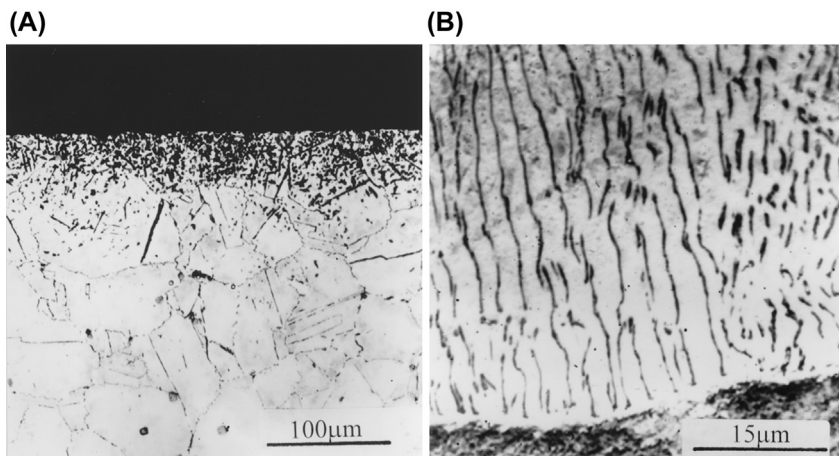


**FIGURE 9.2** Internal carburisation of Fe-Cr at 1000°C: (A) Fe-7.5Cr forms  $M_7C_3$  precipitates and (B) Fe-17Cr forms innermost zone of  $M_{23}C_6$  precipitates [14]. Published with permission from The Electrochemical Society.

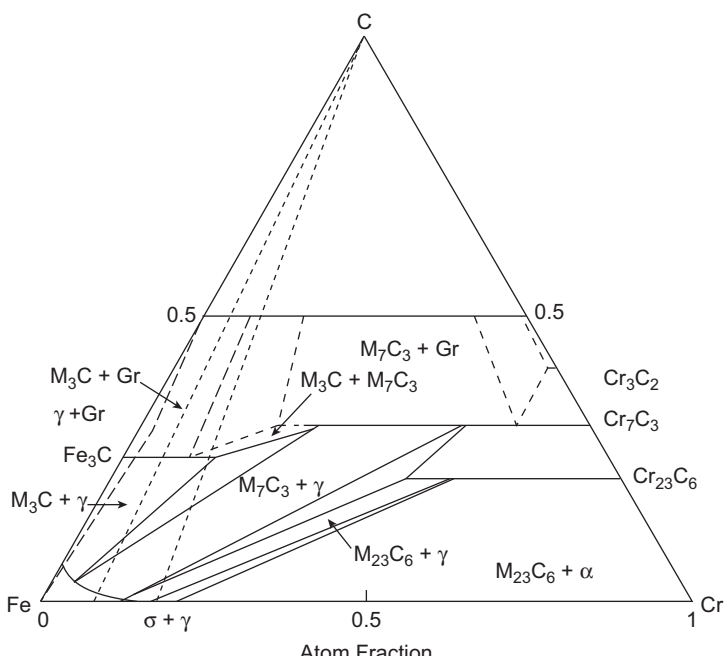


**FIGURE 9.3** Isothermal section at 1000°C of the Fe-Cr-C phase diagram, with dotted lines showing carburisation diffusion paths for  $D_C \gg D_{Cr}$ .

diffusion path which crosses successive two-phase regions  $\gamma + M_{23}C_6$  and  $\gamma + M_7C_3$  before entering the single-phase  $M_7C_3$  field. Again, this corresponds with the experimental observation (Table 9.8) of two internal precipitation zones, with  $M_{23}C_6$  forming in the inner (lower  $a_C$ ) zone.

Because iron solubility in the carbides increases with  $a_C$ , the Fe/Cr ratio in the precipitates is predicted to decrease with increasing depth within the precipitation zone. Microanalysis in a transmission electron microscope of carbides precipitated within an Fe-Ni-Cr alloy [16] revealed the partitioning of chromium between precipitate and matrix in the carburised alloy. As seen in Fig. 9.4, the results are in reasonable agreement with measured equilibrium values, and again it is concluded that local equilibrium is achieved throughout the precipitation zone. Two more important inferences can be drawn from the phase diagram of Fig. 9.3. Carburisation is predicted to transform the alloy matrix of a high chromium Fe-Cr alloy from ferrite to austenite as a result of chromium depletion and carbon saturation. As shown in Fig. 9.2, this transformation is observed at the precipitation front. Secondly, if  $N_{Cr}^{(o)}$  is less than about 0.4, then  $(Fe,Cr)_3C$  is predicted to form at or near the alloy surface if the gas-phase  $a_C$  value is high enough. This is important in metal dusting reactions (Section 9.6) but can be ignored when studying carburisation reactions at  $a_C \leq 1$ . Furthermore, in austenitic alloys the nickel content destabilises  $Fe_3C$ , and the phase is not observed.

#### 9.4.2 Carburisation Kinetics

Internal carburisation is a particular form of internal oxidation, and its kinetics can therefore [6–8,12] be described using Wagner's theory [9], which was

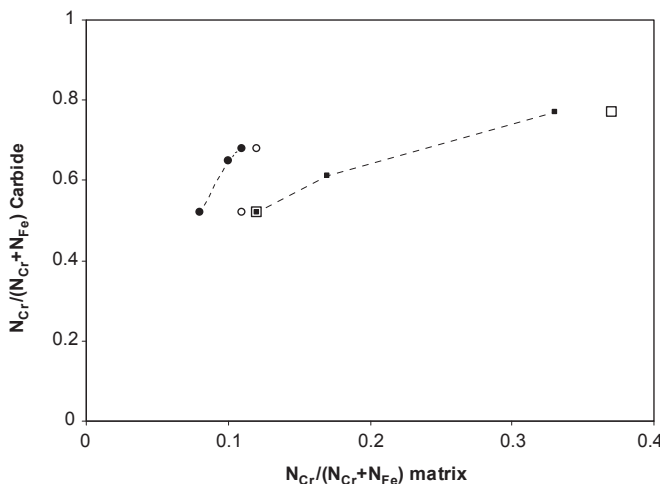


**FIGURE 9.4** Partitioning of Cr between precipitates and matrix in carburised alloy [16,18] (filled symbols) and in equilibrium studies [15] (open symbols).

described in Chapter 6. Because (Table 9.5) carbon permeabilities are so high,  $N_C^{(s)} D_C \gg N_{Cr}^{(o)} D_{Cr}$ , and the rate at which the carbide precipitation zone deepens is given by

$$X_i^2 = 2k_p^{(i)} t \quad [9.23]$$

$$k_p^{(i)} = \frac{\varepsilon N_C^{(s)} D_C}{v N_M^{(o)}} \quad [9.24]$$

where  $N_M^{(o)}$  is the original alloy concentration of metal M, which forms carbide  $MC_v$ . Thus carburisation rates are predicted to vary inversely with concentration of reactive solute metal. Carburisation of Fe-Cr alloys [14,17] follows parabolic kinetics (Fig. 9.5), and plots of  $k_p^{(i)}$  against  $1/N_{Cr}^{(o)}$  are seen to be linear except at high  $N_{Cr}^{(o)}$  values. The slopes of these lines were used together with  $v = 0.71$  (for  $(Cr_{0.6}Fe_{0.4})_7C_3$  formed by low chromium alloys) and the assumption  $\varepsilon = 1$  to calculate carbon permeabilities. Comparison in Table 9.9 with values found from  $N_C^{(s)}$  [2] and  $D_C$  [4] measurements shows good agreement, demonstrating the utility of Eq. [9.24] in describing carburisation rates. This is at first sight somewhat surprising, as Eq. [9.24] is based on the assumption  $K_{SP} \ll 1$ , and the concentration of chromium in the matrix being close to zero. However, as will be seen in the Section 9.4.3 *Carbide Microstructures and Distributions*, the resulting effect on carburisation rates is small.

A further prediction of Eq. [9.24] is that carburisation rates are determined by the permeability of the metal matrix, regardless of the identity of the precipitating carbide, providing that changes in the stoichiometric coefficient  $v$  are taken into account. Permeability values calculated for nickel by Allen and Douglass [12] from their carburisation measurements of Ni-V, Ni-Cr and Ni-Nb alloys are seen in Table 9.10 to be in approximate agreement with each other and with values found from independently measured values of  $N_C^{(s)}$  [3] and  $D_C$  [5]. It is concluded that internal carburisation of both Fe- and Ni-base alloys is controlled by lattice diffusion of carbon through the depleted metal matrix.

The temperature effect on the rate is described by the empirical equation

$$k_p^{(i)} = k_o^{(i)} \exp(-E_A/RT) \quad [9.25]$$

Logarithmic differentiation of Eqs [9.24] and [9.25] yields

$$E_A = \Delta \overline{H}_C + Q \quad [9.26]$$

where  $Q$  is the activation energy of carbon diffusion. In the case of Fe-Cr alloys, the extent of iron dissolution in the carbides varies with temperature as does the stability of the carbides, and the simple description of Eq. [9.26] cannot be expected to apply. In the case of Ni-Cr alloys, however, nickel dissolves to only a small extent in the carbides, and  $Cr_7C_3$  is the only stable

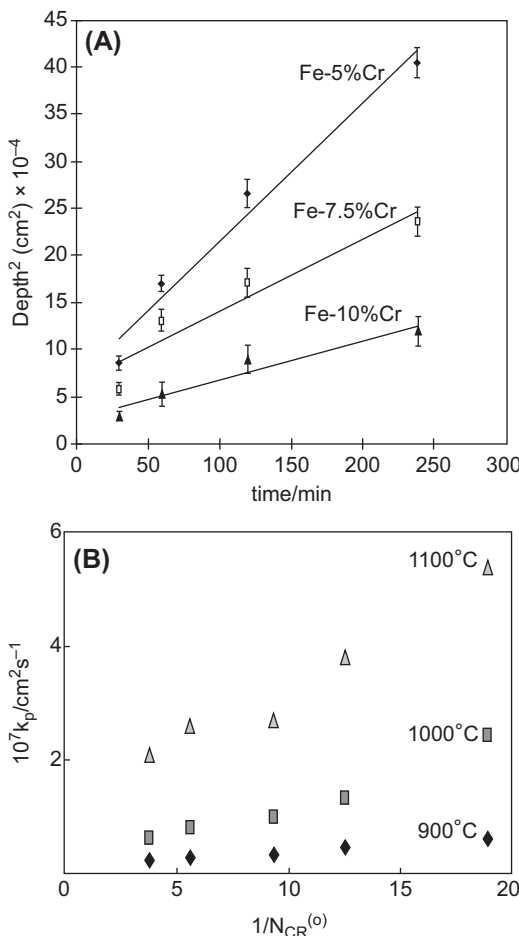


**FIGURE 9.5** Carburisation of Fe-Cr alloys: (A) representative kinetics at 1000°C [14] (*published with permission from The Electrochemical Society*) and (B) effect of alloy chromium content on carburisation rate [17]. (*With permission from Trans Tech Publications, Ltd.*)

internal carbide over a wide range of temperature for  $N_{\text{Cr}}^{(o)} \approx 0.2$ . The value of  $E_A = 190 \text{ kJ mole}^{-1}$  measured by Allen and Douglass [12] for Ni-20Cr agrees with the prediction of Eq. [9.26] based on  $\Delta\overline{H}_C = 54 \text{ kJ mole}^{-1}$  [3] and  $Q = 138 \text{ kJ mole}^{-1}$  [5].

**TABLE 9.9** Carbon Permeabilities  $N_C^{(s)} D_C / \text{cm}^2 \text{ s}^{-1}$  in Fe-Cr

	900°C	1000°C	1100°C
Carburisation kinetics [9.24]	$6.6 \times 10^{-9}$	$2.5 \times 10^{-8}$	$6.2 \times 10^{-8}$
From $N_C^{(s)}$ and $D_C$	$4.3 \times 10^{-9}$	$1.4 \times 10^{-8}$	$5.5 \times 10^{-8}$

**TABLE 9.10** Carbon Permeabilities ( $10^{10} N_C^{(s)} D_C / \text{cm}^2 \text{ s}^{-1}$ ) Deduced [12] From Carburisation Kinetics of Ni-Base Alloys

Alloy	$T/\text{ }^\circ\text{C}$			
	700	800	900	1000
Ni-12V	0.40	2.2	11	44
Ni-20Cr	0.21	0.8	8	55
Ni-3Nb	0.30		6	14
From $N_C^{(s)}$ and $D_C$	0.19	1.6	7	36

Chromia-forming alloys are usually based on Fe-Ni (Table 9.1), and the applicability of Eq. [9.24] to Fe-Ni-Cr model alloys is now tested. An Fe-20Ni-25Cr alloy carburised at 1000°C and  $a_C = 1$  is seen in Fig. 9.6 to have developed a near-surface zone of  $\text{M}_7\text{C}_3$  precipitates and an inner zone containing  $\text{M}_{23}\text{C}_6$ . Carburisation kinetics of a series of Fe-Ni-Cr alloys have been found [19] to be parabolic at 1000°C, and the rate constants are seen in Fig. 9.7 to vary considerably with alloy nickel content. If nearly all the chromium is precipitated as carbide, then the reaction is sustained by carbon

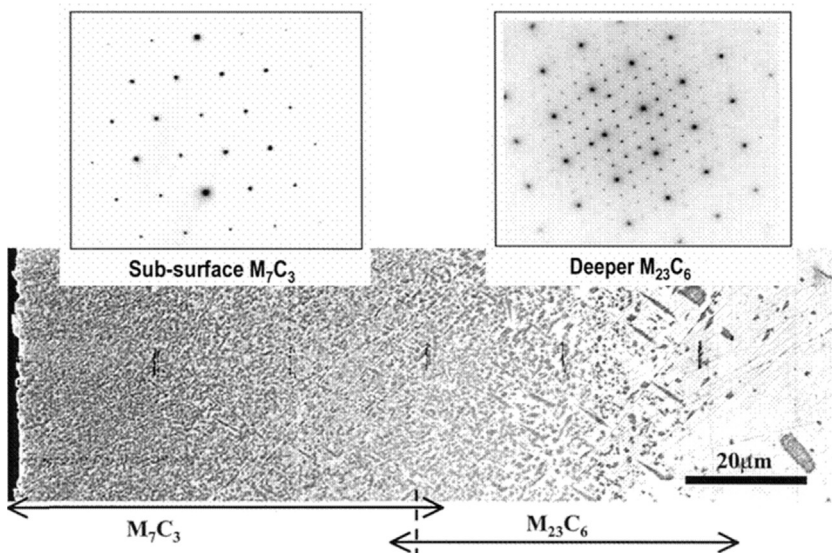


**FIGURE 9.6** Carburisation of Fe-20Ni-25Cr at 1000°C, and  $a_C = 1$ . Precipitates in the sub-surface zone are  $\text{M}_7\text{C}_3$ , and in the inner zone,  $\text{M}_{23}\text{C}_6$  [18]. With permission from ASM International.

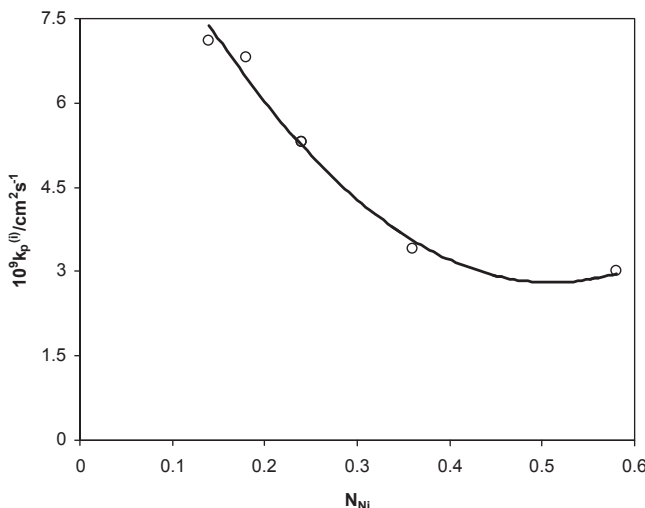


**FIGURE 9.7** Variation of carburisation rate at 1000°C with Ni content of Fe-Ni-25Cr alloys.  
Reprinted from M. Udyavar; D.J. Young, Corros. Sci. 42 861 (2000) with permission from Elsevier.

dissolution in and diffusion through the remaining Fe-Ni matrix. Ignoring the dissolution of some of the iron into carbide, we approximate the matrix as having the same  $N_{Ni}/N_{Fe}$  ratio as the parent alloy. On this basis, one can use values of  $N_C^{(s)}$  measured by Wada et al. [3] for Fe-Ni alloys and for  $D_C$  measured by Bose and Grabke [10] to predict carburisation rates from Eq. [9.24]. A comparison of measurement and prediction (Fig. 9.8) demonstrates the success of this procedure. It is therefore concluded that the Wagner theory provides a satisfactory basis for describing the carburisation of model alloy compositions close to those of commercial heat-resisting alloys. Before going on to consider more practical alloys, we consider the microstructures and distributions of carbide precipitates.

#### 9.4.3 Carbide Microstructures and Distributions

Particles of  $M_7C_3$  precipitated in austenite are globular and develop no rational orientation relationship with the matrix. In contrast,  $M_{23}C_6$  possesses a cubic structure and develops a strong cube-in-cube orientation relationship with the *fcc*  $\gamma$ -matrix [21]

$$[001]_\gamma \parallel [001]_{M_{23}C_6} : (100)_\gamma \parallel (100)_{M_{23}C_6} \quad [9.27]$$

Usually the  $M_{23}C_6$  precipitates are small, cuboidal or needle-shaped particles (eg, Fig. 9.9). The small size of the precipitates reflects the fact that they grew for only a short time: a result of the continued nucleation of new carbide particles as the reaction front advanced into the alloys. This in turn was due to

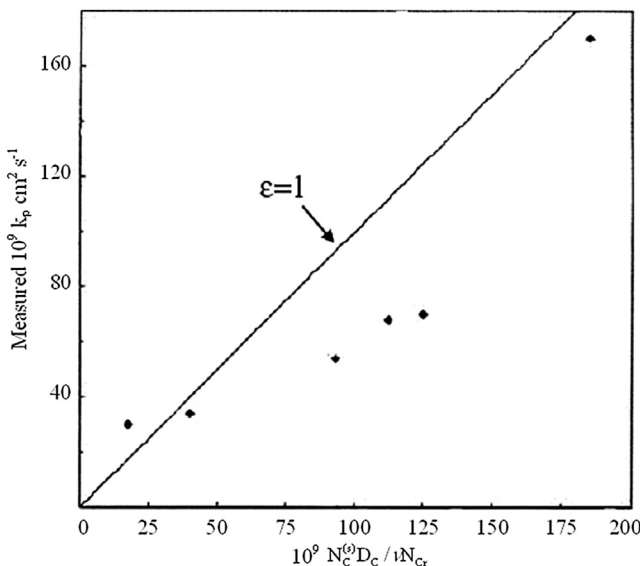
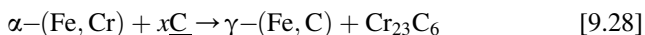


**FIGURE 9.8** Measured carburisation rates of Fe-Ni-Cr alloys compared with values calculated from diffusion model. Reprinted from M. Udyavar, D.J. Young, *Corros. Sci.* 42 861 (2000) with permission from Elsevier.

rapid carbon diffusion, which quickly produced sufficient supersaturation to favour homogeneously distributed nucleation. In other circumstances, the same carbide can form elongated lamellar- or lath-shaped precipitates oriented parallel to the reaction direction (Fig. 9.9). Because the value of  $k_p^{(i)}$  is 30–50% higher when the aligned microstructure is adopted, the reasons for its development are of interest.

Lamellar or cellular  $M_{23}C_6$  microstructures have been reported to develop in ferritic alloys [14,16,22,23], in high nickel austenitics [19] and in a variety of heat-resisting alloys carburised at low temperatures [24,25]. They are also observed in previously nitrided Fe-Ni-Cr alloys [19,21]. A distinctive feature in all cases is the formation of a grain boundary at the carbide precipitation front. In the case of ferritic alloys (Fig. 9.2B) the boundary corresponds to the phase transformation



In high nickel alloys, lamellar carbides develop in colonies in the alloy interior. It seems likely that they nucleated at alloy grain boundaries and then grew into the adjacent grain in a discontinuous precipitation process, which is now described.

A brief period of internal nitridation can be used to form a boundary just beneath the surface of an Fe-Ni-Cr alloy (Section 6.7). Subsequent carburisation then leads to rapid inward growth of  $M_{23}C_6$  lamellae, which advances

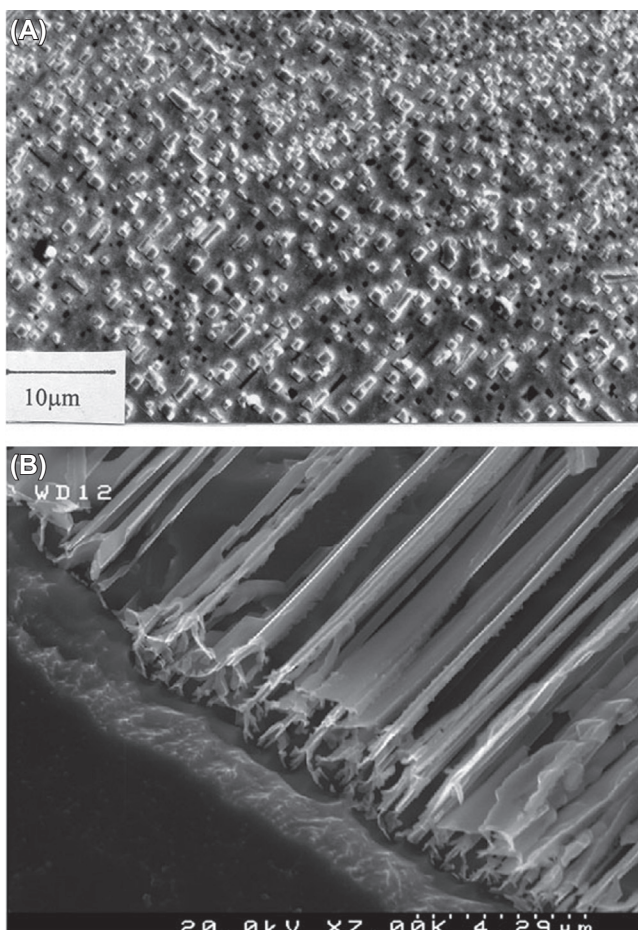


**FIGURE 9.9** Cuboidal (A) and lath-shaped (B)  $M_{23}C_6$  precipitates at the reaction front in Fe-20Ni-25Cr carburised at 1000°C.

the boundary. A high magnification view of the reaction front is shown in Fig. 9.10: the dark grain on the right is unreacted austenite, the light grain on the left is chromium-depleted matrix and the precipitates are  $M_{23}C_6$ . The selected area diffraction pattern shows the same cube-in-cube orientation relationship [9.27] between precipitate and matrix. The crystallographically oriented sides of the precipitates were always the close-packed (111) planes. No rational orientation relationships were found between unreacted austenite and either reacted austenite or carbide. Microanalysis results in Fig. 9.10 show a step function change in  $N_{Cr}$  at the austenite/depleted austenite grain boundary, but no sign of lateral diffusion within the matrix. The mechanism is that of discontinuous precipitation [18,21]

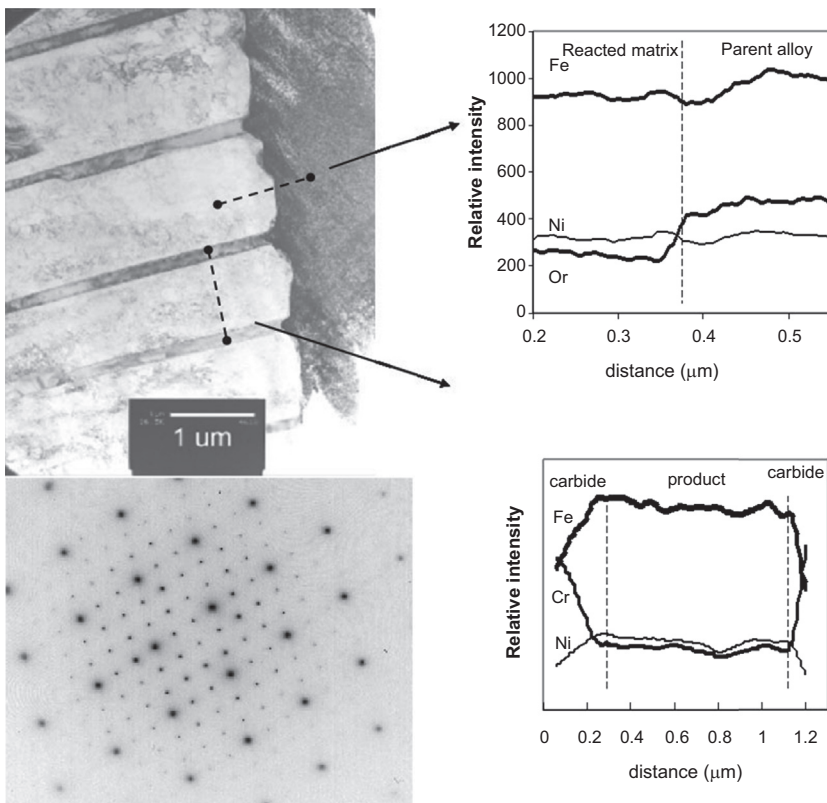


**FIGURE 9.10**  $M_{23}C_6$  precipitation front in Fe-20Ni-25Cr after brief prenitridation and subsequent carburisation at  $1000^{\circ}\text{C}$ ,  $a_C = 1$ . SAD shows precipitate/matrix coherency and concentration profiles corresponding to discontinuous precipitation [18,21]. Published with permission from *Science Reviews*.



where  $\gamma^D$  denotes depleted austenite. The change in crystallographic orientation from parent  $\gamma$  to product  $\gamma^D$  is obvious in Fig. 9.10. This reorientation results from the free energy reduction achieved when the austenite forms coherent interfaces with the precipitates which grew approximately unidirectionally, parallel to the carbon diffusion direction. The incoherency of the  $\gamma/\gamma^D$  interface is evident in its curvature, and this provides rapid chromium diffusion towards the advancing carbide precipitate tips, sustaining their growth and producing the discontinuous change in  $N_{\text{Cr}}$  seen at the interface.

It is concluded that lamellar carbide precipitates develop when a grain boundary is present. The boundary provides more rapid chromium diffusion to the precipitates, favouring their continued growth rather than nucleation of

new ones. As seen in Fig. 9.5B, carburisation rates for Fe-Cr alloys with high  $N_{\text{Cr}}$  values are higher than predicted by Eq. [9.24]. These are the alloys which form lamellar precipitates, and the acceleration is attributed to boundary diffusion of carbon along the multiple carbide-austenite interfaces. Because  $N_{\text{C}}^{(\text{s})} D_{\text{C}}$  in austenite is in any case large, the increase in rate is relatively small: 30% faster in Fe-Cr and 30–50% faster in Fe-Ni-Cr alloys at 1000°C.

Carbide precipitate distributions are nonuniform, because  $K_{\text{sp}}$  is not small. Thus as depth within the precipitation zone increases,  $a_{\text{C}}$  and  $N_{\text{C}}$  decrease, causing  $N_{\text{Cr}}$  to increase according to the solubility product equilibria Eqs [9.21] and [9.22]. As a result, the amount of chromium precipitated is less [17]. The qualitative effect on carburisation rate can be seen from Eq. [9.24]: because the effective value of  $N_{\text{Cr}}^{(0)}$  is lowered, the penetration rate is faster. This effect has been analysed [26,27] for the general case of low stability precipitates. Deviation from the Wagner assumption of vanishingly small  $K_{\text{sp}}$  values is expressed via a solubility parameter

$$\alpha = 1 - N_{\text{Cr}}^{(\text{s})} / N_{\text{Cr}}^{(0)} \quad [9.30]$$

where  $N_{\text{Cr}}^{(\text{s})}$  is the matrix equilibrium chromium concentration at the surface of the reacted alloy. If  $\alpha = 1$ ,  $K_{\text{sp}} = 0$  and the Wagner model applies; if  $\alpha = 0$ , no precipitation occurs and an error function solution describes the carbon profile. Considering Fe-Cr alloys, we find from Eq. [9.22] and the data of Table 9.6 that  $N_{\text{Cr}}^{(\text{s})} = 0.028$ . Taking a representative value of  $N_{\text{Cr}}^{(0)} = 0.25$ , then a value of  $\alpha = 0.9$  is arrived at. For this value, Ohriner and Morall [26] calculate that  $k_p^{(i)}$  is increased by a factor of two above that predicted from Eq. [9.24], ie, the penetration depth is increased by about 40%. However, uncertainties in measured values of  $D_{\text{C}}$ ,  $N_{\text{C}}^{(\text{s})}$  and  $k_p^{(i)}$  total at least this amount. A similar conclusion is reached for M<sub>23</sub>C<sub>6</sub> precipitation. It is therefore concluded that despite the approximate nature of its assumptions, the simple result Eq. [9.24] provides good order of magnitude prediction for model alloy carburisation. A more precise prediction can be made using the numerical treatment of the Ohriner–Morall theory developed by Christ [28].

## 9.5 INTERNAL CARBURISATION OF HEAT-RESISTING ALLOYS

Many laboratory studies of the carburisation of heat-resisting alloys have been reported, eg, [6–8,28–44]. These are in general agreement with the findings from industrial exposures (see, eg, Ref. [45]) that carburisation rates vary with Fe/Ni ratio and decrease with increased levels of Cr, Nb, Si and sometimes W and Ti.

The usual appearance of a cast heat-resistant alloy after carburisation is shown in Fig. 9.11. Murakami's etch reveals finely precipitated, cuboidal

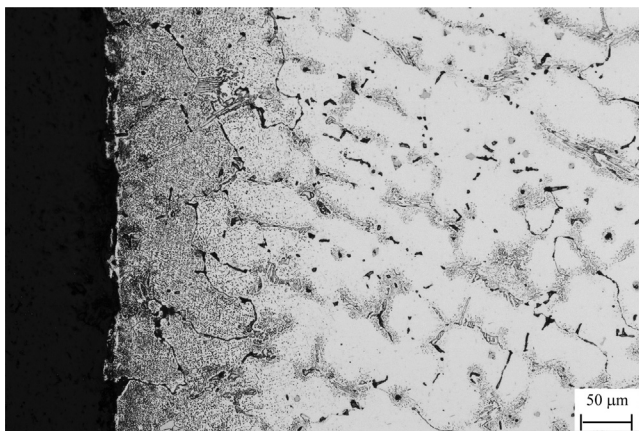


**FIGURE 9.11** Cast alloy 45Pa after carburisation for 24 h at 900°C and  $a_C = 1$ .

$M_{23}C_6$  particles in the inner zone and coarser, spherical  $M_7C_3$  particles near the surface. The original cast alloy structure is seen to the right: austenite dendrites with primary interdendritic  $M_{23}C_6$ . Near the carburisation front, preferential precipitation is seen along dendrite boundaries. Some fragmentary external carbide scale is also seen. This is usually  $Cr_3C_2$  on high-nickel alloys and  $M_7C_3$  on low-nickel materials. The difference arises from the changed Fe/Cr ratios [35] (see Fig. 9.3). Thus reaction morphologies are consistent with local equilibrium. Since, moreover, internal carburisation kinetics are parabolic, it is clear that the process is diffusion-controlled.

Despite the complexity of these alloys, their relative performance under nonoxidising conditions can be understood in terms of Wagner's Eq. [9.24]. The procedure is to model the heat-resisting alloys as Fe-Ni-Cr ternaries and approximate the carburisation zones as chromium carbide precipitates in an Fe-Ni matrix. Carburisation rates are then predicted from Eq. [9.24] to change with carbon permeability,  $N_C^{(s)}D_C$ . This permeability shows a minimum at  $Ni/Fe \approx 4:1$  [3,20,46], which is seen in Fig. 9.12 to be reflected in relative penetration depths of a range of alloys. Clearly the Fe/Ni ratio has a significant effect on carburisation rate. However, it is desirable also to account for the effect of  $N_M$  in Eq. [9.24], and a more detailed calculation is required.

The quantity  $N_M$  represents mainly chromium. In calculating its value, the alloy chromium content must therefore be corrected for the amount already removed from the matrix into interdendritic carbide during casting. This is done on the assumption that all of the alloy carbon was precipitated as pure  $M_{23}C_6$ . Added contributions to  $N_M$  are calculated on the basis of NbC and other MC carbide formation, as well as the molybdenum carbides  $(Mo_2Fe)C$  and  $(CrMoFe)C$ . As seen earlier, the application of Eq. [9.24] is nonetheless an approximation because  $M_7C_3$  and  $M_{23}C_6$  carbides contain substantial levels of iron [15]. Consequently, the value of  $N_m$  calculated as described above is an

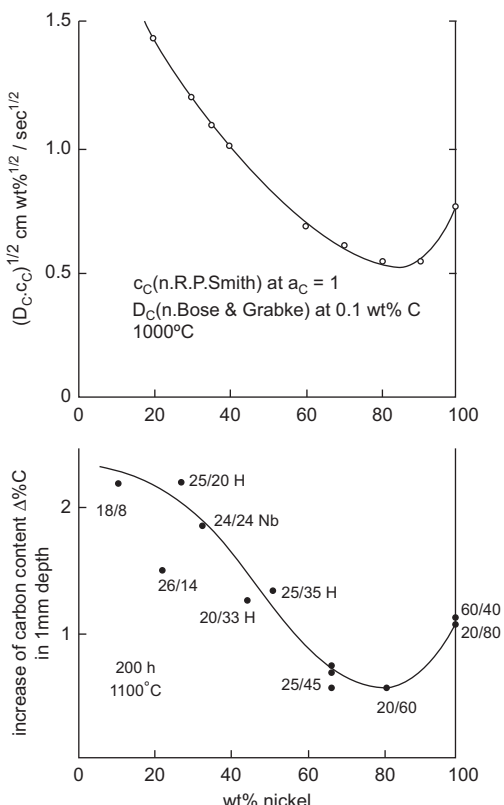


**FIGURE 9.12** Effect of alloy nickel content on (upper) carbon permeability in Fe-Ni and (lower) carburisation extent in 200 h at 1100°C [47]. Published with permission from Wiley-VCH.

underestimate. On the other hand, however, an overestimate of  $N_m$  results from the error in the mass balance underlying Eq. [9.24]. This latter error arises because the solubility products of  $\text{Cr}_7\text{C}_3$  and  $\text{Cr}_{23}\text{C}_6$  are large, and significant levels of chromium remain unreacted in the depleted matrix.

Carburisation leads to approximately equimolar amounts of  $\text{M}_7\text{C}_3$  and  $\text{M}_{23}\text{C}_6$ , so a value of  $v = 0.345$  is used in Eq. [9.24]. No value for  $\epsilon$  is available. Predicted  $k_p$  values based on  $\epsilon = 1$  are compared in Table 9.11 with measured [40] quantities for a selection of alloys. It is seen that close order of magnitude agreement is achieved for the 30, 35 and 45 Ni grades, but not for the 60 Ni grades. The latter contain aluminium and are discussed below. We consider first the effects of other alloy components.

### 9.5.1 Effect of Carbon

As seen in Table 9.1, cast alloys usually contain high levels of carbon, which segregates as  $\text{M}_{23}\text{C}_6$  during alloy solidification, thereby affecting  $N_m$  as described above. The success of this description is tested by comparing

**TABLE 9.11** Carburisation Rate Constants ( $10^7 k_p/\text{cm}^2 \text{ s}^{-1}$ ) [40]

	(1100°C)		(1000°C)		(900°C)	
	Measured	Calc	Measured	Calc	Measured	Calc
G4868	1.45	2.05	0.13	0.33	0.10	0.11
G4852	0.64	2.15	0.28	0.37	0.18	0.10
H101	0.44	1.32	0.17	0.24	0.06	0.06
Fe-35Cr-45Ni	0.44	0.50	0.10	0.08	0.04	0.03
45Pa	0.41–0.43	0.99	0.13–0.22	0.18	0.05–0.08	0.034
45HT	0.63	0.62	0.10–0.15	0.15	0.04–0.05	0.023
60HT <sup>b</sup>	0.14	0.87	0.04	0.17	0.03	0.03
60HT <sup>b</sup>	0.01	0.95	0.01	0.19	0.02	0.03
60HT <sup>b</sup>	0.02	0.90	nd <sup>a</sup>	0.18	nd <sup>a</sup>	0.03
602CA	0.14	0.82	0.04	0.17	0.03	0.03

<sup>a</sup>nd: not determined.<sup>b</sup>Low, medium and high  $N_{\text{Al}}$  (Table 9.1)

carburisation rates for alloys H101 and G4582, which differ in their carbon levels but are otherwise similar. At 1000°C, the ratio  $k_p(\text{G4582})/k_p(\text{H101})$  predicted from Eq. [9.24] to be 1.5 compares well with the measured value of 1.7. Agreement at the other temperatures is also good. It is concluded that the method used to calculate the effect of original alloy carbon is successful. On this basis, it would follow that cast alloys have lower carburisation resistance than their wrought (low carbon) equivalents. In fact, the opposite effect is found [8,38] as a result of rapid grain boundary diffusion of carbon in wrought alloys.

### 9.5.2 Effect of Molybdenum

Molybdenum can be added for solution strengthening of an alloy, and is also a carbide former. Two alloys containing 24 Cr, 32 Ni, 0.8 Nb and 0.44 C, with and without additions of 3 wt% Mo were found [38] to carburise at  $a_{\text{C}} = 1$  at different rates. The carbides  $\text{Mo}_3\text{C}$  and  $\text{Cr}_7\text{C}_3$  are of comparable stability and can therefore coexist if the metals are at similar activity levels. In fact the carbides  $(\text{Mo}_2\text{Fe})\text{C}$ ,  $(\text{CrFeMo})\text{C}$  and  $\text{Cr}_7\text{C}_3$  were all identified by X-ray diffraction analysis of the carburised alloy. The possibility that precipitation of molybdenum carbides slows the rate is tested using Eq. [9.24].

A level of 3 w/o molybdenum, forming a carbide of stoichiometry  $\text{Mo}_{1.5}\text{C}$  (an average of the two observed carbides), is equivalent in its consumption of carbon to a level of 2.5 w/o chromium, forming  $\text{Cr}_7\text{C}_3$ . The value of  $N_m$  in the

alloy with 3% Mo is on this basis calculated to be 13.6% higher than for the alloy with none. Taking into account the effects of alloy compositional changes in  $D_C$ ,  $N_C$  and  $N_m$  gives predicted relative reductions in the  $k_p$  values for the molybdenum-containing alloy of 40% at 900°C, 23% at 1050°C and 10% at 1150°C. The measured reductions were 44% at 900°C, 24% at 1050°C and 16% at 1150°C. This shows that Eq. [9.24] enables the effect of molybdenum to be modelled, subject to the reliability of the  $N_C$  and  $D_C$  data. Furthermore, it also predicts correctly the effect of temperature on the efficacy of this element in reducing carburisation.

### 9.5.3 Effect of Silicon

It has long been known [29] that silicon slows carburisation, even under gas conditions where no silicon-rich oxide can form. The stability of SiC is a great deal less than that of Cr<sub>23</sub>C<sub>6</sub> and C<sub>7</sub>C<sub>3</sub>, and no SiC will form in these chromium-rich alloys. Increasing the alloy silicon content therefore has no effect on  $N_m$ . Under reducing conditions, no SiO<sub>2</sub> is formed, and the beneficial effects to be expected of silicon on carburisation rates must therefore result from modification of the carbon solubility and/or diffusivity. These changes are due to thermodynamic interaction between the dissolved silicon and carbon.

Silicon is known to reduce both  $N_C^{(s)}$  and  $D_C$ . Roy et al. [48] have examined the effect of silicon on carbon diffusion in Fe-Si-C. A comparison of carburisation rates of two cast heat-resisting steels which differed only in their silicon levels showed [38] that increasing the silicon level decreased the rate by more than would be predicted from Roy's diffusion data. The other major contributory factor is the depression of carbon solubility by silicon. The effect has been measured in liquid iron alloys, where the resulting change in carbon solubility is significant, but no data directly applicable to heat-resisting alloys are available.

### 9.5.4 Effect of Niobium and Reactive Elements

Niobium is often added to cast heat-resistant alloys for strengthening purposes. It is also found in some wrought alloys, where it improves weldability. Reactive elements such as Ce and Hf are added to modify carbide shapes and to improve oxide scale spallation resistance. All are strong carbide formers and have strong effects on carburisation resistance. The benefits of niobium have been reported several times [8,45,49]. The variation of  $k_p^{(i)}$  with niobium concentrations is shown in Fig. 9.13 for several heat-resisting alloys. The effect of niobium can be distinguished from variations in  $N_C^{(s)}C_C/D_m$ , also plotted in this figure. Even if all the alloy niobium was available in solution to precipitate NbC, the effect of adding 1–2 w/o Nb on  $N_m$  is very small, much less than the substantial reductions in  $k_p^{(i)}$  seen at higher niobium levels.

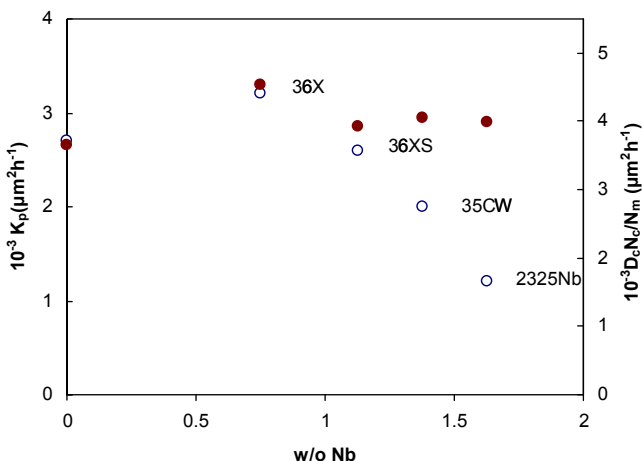


**FIGURE 9.13** Carburisation rate constants for commercial 25Cr-35Ni alloys at 1000°C as a function of niobium content (○) compared with  $N_C^{(s)} D_C / N_M$  (●) [8]. With kind permission from Springer Science and Business Media.

Similar effects have been noted for additions of Ce [39] and Hf [40]. These elements are present at low concentrations, typically around 0.1–1.0 w/o, and their effect on the value of  $N_m$  is negligible. Nonetheless their addition is found to reduce carburisation rates substantially. It is possible that carbides of Nb, Ce and Hf precipitate preferentially at sites where interference with carbon diffusion is maximal. As carbon penetration is more rapid at primary carbide/dendrite boundaries (Fig. 9.11), reactive metal carbide precipitation at these interfaces could exercise a disproportionate effect on the overall rate.

### 9.5.5 Effect of Aluminium

The 60 Ni alloys in Table 9.11 were predicted from Eq. [9.24] to carburise at rates similar to the 45 Ni alloys. At 900°C, the wrought alloy 602 CA and two cast versions reacted at close to the predicted rates. At higher temperatures, the rates were much slower than predicted. The explanation is clear from the micrographs of Fig. 9.14, where a protective, external scale is seen to form on high  $N_{\text{Al}}$  alloys. The scale was  $\alpha\text{-Al}_2\text{O}_3$ , which is thermodynamically stable at the water vapour impurity levels which are unavoidable in reaction gases. However, external scale formation is possible only when a sufficient flux of alloy solute aluminium is available, and internal oxidation can be avoided (see Fig. 9.14). This flux increases with both alloy  $N_{\text{Al}}$  and temperature, through its effect on  $D_{\text{Al}}$ , qualitatively accounting for the observed pattern of behaviour. When this scale forms, it functions as a barrier, limiting carbon access to the underlying metal. Thus at 900°C, no alumina formed, and the 60Ni alloys all carburised at the expected rates. At 1000 and 1100°C, alumina scales grew on

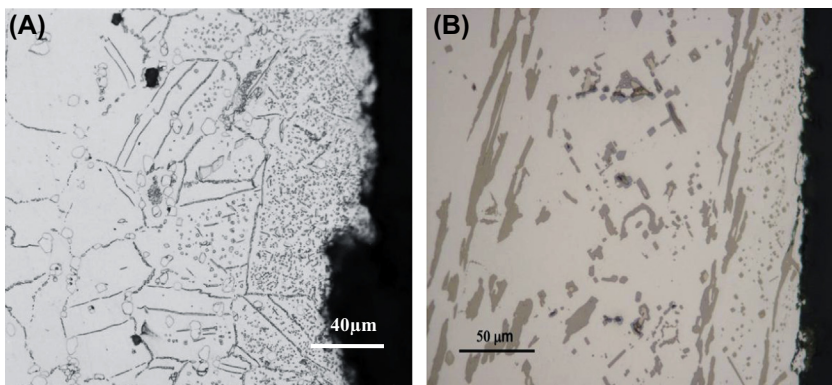


**FIGURE 9.14** Effect of  $\text{Al}_2\text{O}_3$  formation on 60Ni alloys: (A) low Al at  $900^\circ\text{C}$  and (B) high Al at  $1100^\circ\text{C}$ .

all alloys, and carburisation was slowed. The scale was discontinuous on the low aluminium alloys, and carburisation was not completely suppressed. A minimum aluminium content of about 4 w/o was required to achieve complete protection.

### 9.5.6 Alloying for Carburisation Protection

The kinetics of alloy carburisation are very well described by diffusion theory, and a rational approach to alloy design is therefore available. Unfortunately, however, most methods of suppressing internal attack on chromia-forming alloys are either impractical or only modestly successful. It is not possible to adjust chromium levels to achieve exclusive external carbide growth. Modifications of alloy carbon permeability through adjusting the Fe/Ni ratio or alloying with other metals yield only small improvements in carburisation rates. Silicon decreases carbon solubility and diffusivity quite strongly, but metallurgical limits on alloy silicon concentrations mean that only modest improvements in carburisation resistance can be obtained. The only really successful alloy additive is aluminium, and it functions by forming an oxide scale. The general question of protection against carburisation by oxide scale formation is considered in [Section 9.8](#).

## 9.6 METAL DUSTING OF IRON AND FERRITIC ALLOYS

Metal dusting is a catastrophic form of corrosion in which metals exposed to carbon-supersaturated gas disintegrate, forming metal-rich particles (the ‘dust’) dispersed in a voluminous carbon deposit. Early reports of industrial failures [50–53] were followed by the laboratory research of Hochman [54–56] concerning the dusting of iron, nickel, cobalt and chromia-forming ferritic and austenitic alloys. Subsequently, work by Grabke [57–61] quantified and

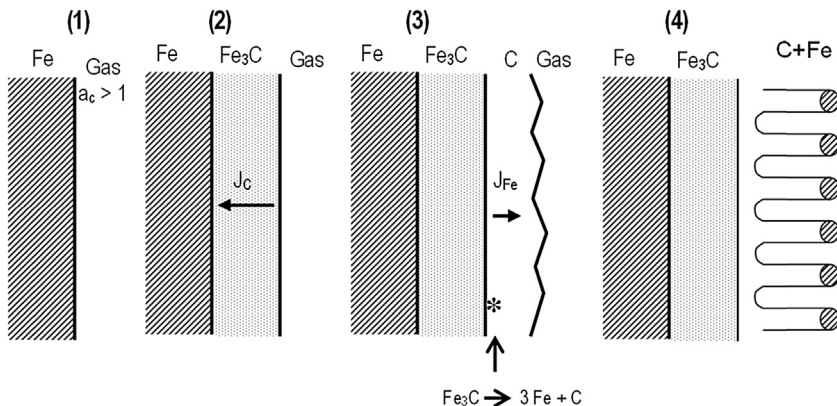


FIGURE 9.15 Hochman—Grabke model for dusting of pure iron.

extended Hochman's observations. The description of the process, as provided by Hochman and Grabke, for pure iron is shown schematically in Fig. 9.15.

### 9.6.1 Metal Dusting of Iron

When iron is exposed to carbon-rich gas at oxygen potentials too low to form iron oxide, the metal catalyses reactions such as Eqs [9.7–9.9], but the resulting carbon is dissolved in the metal. Hochman and Grabke suggested that this leads to carbon supersaturation of the iron, and the subsequent precipitation of the metastable  $\text{Fe}_3\text{C}$  phase, which they observed. The appearance of the cementite is shown in Fig. 9.16. According to the proposed mechanism, once the iron surface is covered with cementite, carbon deposits on the carbide. The carbon activity at the cementite surface is then supposed to be unity (rather than the supersaturated value of the gas phase); the cementite becomes unstable and decomposes via the reaction



producing finely divided iron and carbon. The iron particles produced in this way are catalytically active and lead to accelerated carbon deposition. The resulting conglomerate deposit of carbon and metal-rich particles is at least 95% carbon and is referred to as ‘coke’, and the carbon deposition process as coking. The shortcomings of this mechanism are analysed below.

The kinetics of carbon deposition were observed [61] in the short term to follow the quadratic rate law

$$\Delta W_{\text{C}}/A = k_{\text{C}} t^2 \quad [9.32]$$

where  $\Delta W_{\text{C}}/A$  is the carbon weight per unit area, before becoming approximately linear. The form of Eq. [9.31] was explained by Grabke et al. [61] as

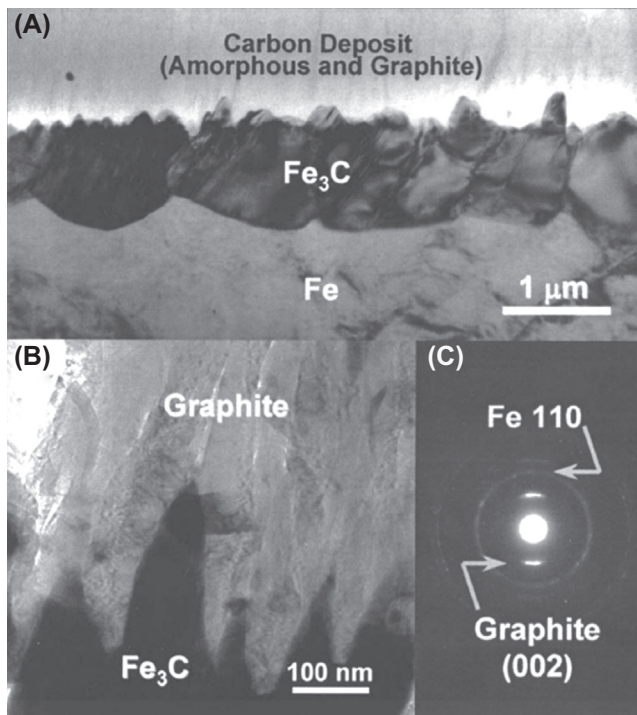


**FIGURE 9.16** Cross-sectional TEM views showing Fe/Fe<sub>3</sub>C/C interfaces after reaction in CO/H<sub>2</sub> at 650°C [65]. Published with permission from The Electrochemical Society.

being due to the generation of catalytically active particles by metal consumption in the dusting process:

$$\Delta W_m/A = k_{dt} \quad [9.33]$$

where  $\Delta W_m/A$  is the metal wastage expressed as a mass loss per unit area. If the catalytic particles are of uniform surface area and activity, then the rate of carbon deposition is proportional to the mass of metal consumed

$$\frac{d(\Delta W_C/A)}{dt} = k \cdot k_{dt} \quad [9.34]$$

Integration of this expression yields Eq. [9.32]. In the long-term, individual particles are encapsulated by carbon and deactivated as catalysts. The rate at which this happens is suggested to approximately balance the rate of new particle generation, and coking rates become approximately constant.

Transmission electron microscopy [63–66] has revealed that the carbon at the cementite surface is mainly graphite at temperatures above about 500°C (Fig. 9.16). It was suggested that the iron resulting from cementite decomposition dissolved in the graphite, diffused outwards and precipitated as metal

particles which catalysed further carbon deposition. The evidence for this was the measurement by EDS of a small concentration of iron in the graphite. However, it is difficult to understand the driving force which would cause iron to diffuse from a low-activity source, the cementite, towards a high-activity destination, metallic iron particles.

Further examination of the particles by both X-ray and electron diffraction [24,67–70] has established that they are actually  $\text{Fe}_3\text{C}$ . As seen in Fig. 9.17, much of the coke deposit is filamentary. These filaments are multiwall carbon nanotubes and usually carry faceted  $\text{Fe}_3\text{C}$  particles at their tips. The particles are oriented with their [001] direction parallel to the carbon tube axis [71]. This allows  $\text{Fe}_3\text{C}$  planes in the {010} and {100} families to be parallel to the tube axis. The d-spacing of the (020) plane is 0.337 nm and that of the (300) plane is 0.169 nm. These correspond closely to the (0002) and (0004) d-spacings of graphite (0.337 nm and 0.168 nm, respectively). Accordingly, it is suggested that alignment of these planes with the graphite basal planes, which form the multiple walls of the nanotube, leads to formation of low energy graphite-carbide interfaces and a preferred growth orientation for the carbon nanotubes.

A mass transport model for filamentary coke deposition is shown in Fig. 9.17C. The exposed  $\text{Fe}_3\text{C}$  facets are in contact with the gas, and catalyse

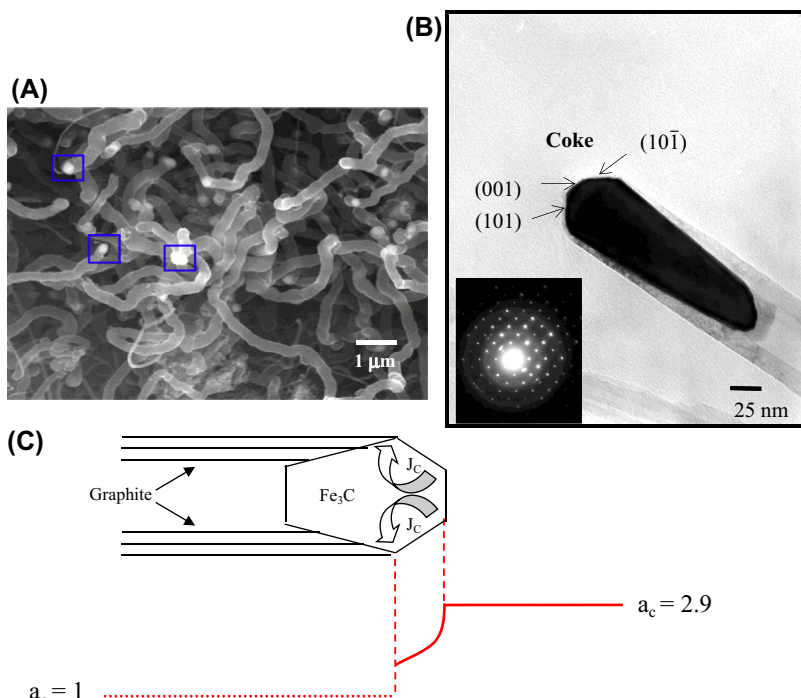


**FIGURE 9.17** Coke filaments with  $\text{Fe}_3\text{C}$  particles at their tips (thin): (A) SEM view, (B) TEM bright field image and SAD pattern and (C) mass transfer model.

carbon production. This carbon diffuses through the particle to the  $\text{Fe}_3\text{C}$ -graphite interface where growth of the attached carbon nanotube continues. Thus the cementite crystallites perform three functions: catalysis of the gas reaction, dissolution and transport of the resulting carbon, and provision of a template for graphite nucleation and growth. The model is analogous, with respect to the first two functions, to that originally proposed by Baker et al. [72] for catalysis of carbon filaments grown by metallic particles. There remains, however, the question of how the cementite particles are formed.

If iron did in fact dissolve in graphite, it could diffuse outward if a carbon activity gradient was in effect, as illustrated in Fig. 9.18A. The iron flux would be given by

$$J_{\text{Fe}} = B_{\text{Fe}} N_{\text{Fe}} \frac{\partial \mu_{\text{C}}}{\partial x} \quad [9.35]$$

as a result of the thermodynamic Fe-C interaction. Here  $B_{\text{Fe}}$  is the mobility of iron in graphite. When the solute iron reached a position at which  $a_{\text{C}}$  was high enough to stabilise cementite, that phase would precipitate. To test this model,

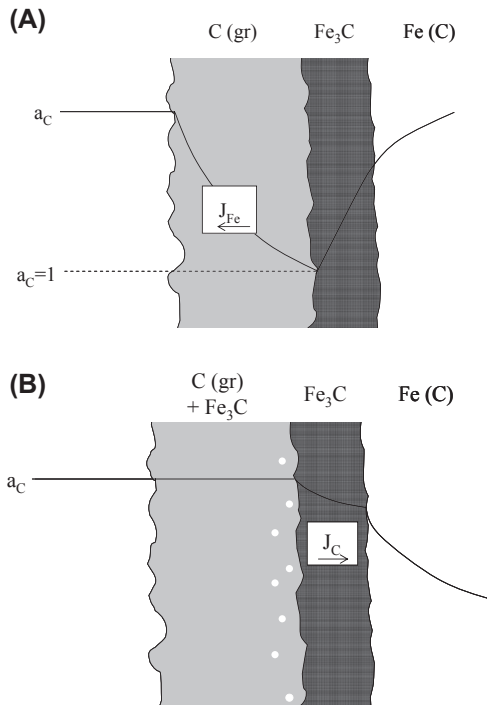


**FIGURE 9.18** Mass transport models for metal dusting when cementite is formed: (A) cementite *decomposition* and iron diffusion through graphite [63–65] and (B) cementite *disintegration* coupled with inward carbon diffusion [67,79].

one needs values for iron solubility and its diffusion coefficient in graphite, and these are lacking. It is clear that an extremely high value for  $D_{\text{Fe}}$  would be required to explain why the decomposition reaction (Eq. [9.31]) leads to 75 atom percent iron but produces none of that phase at the decomposition site.

A more fundamental difficulty arises with the Hochman–Grabke model. The coke deposit is not a single-phase solid solution: as seen above, it is actually a mixture of carbon and  $\text{Fe}_3\text{C}$  particles. No activity gradient can exist in a two-component ( $\text{Fe} + \text{C}$ ), two-phase mixture; solid-state diffusion is therefore impossible and the model fails.

Studies of cementite decomposition in  $\text{CH}_4\text{-H}_2$  gas mixtures [73] have shown that the reaction products are iron and graphite. In that case, however, the iron forms as a bulk phase, not as particles. The reaction is controlled by the diffusion of carbon through the product ferrite, driven by the carbon activity gradient between the high value at the  $\text{Fe}_3\text{C}/\text{Fe}$  phase boundary and its value of unity at the  $\text{Fe}/(\text{C(gr})$  boundary. According to Fick's law:

$$\text{Rate} = D_C \left( C^{\text{Fe}_3\text{C}/\text{Fe}} - C^{\text{C}/\text{Fe}} \right) \quad [9.36]$$

where  $C^{\text{Fe}_3\text{C}/\text{C}}$  and  $C^{\text{C}/\text{Fe}}$  are carbon concentrations at the ferrite-cementite and ferrite-graphite interfaces,  $D_C$  is the carbon diffusion coefficient in ferrite, and variation in the diffusion path length is ignored. The concentration of carbon is related to its activity by a coefficient  $\gamma_C$ , with  $a_C = \gamma_C C$ . Approximating  $\gamma_C$  as a constant and setting  $a_C = 1$  at the iron-graphite interface, we obtain

$$\text{Rate} = D_C \left( a_C^{\text{Fe}_3\text{C}/\text{Fe}} - 1 \right) / \gamma_C \quad [9.37]$$

Using standard data for  $D_C$  [74] and  $a_C^{\text{Fe}_3\text{C}/\text{Fe}}$  [75], it is found that the temperature dependence of cementite decomposition predicted by Eq. [9.37] is in very good agreement with experimental observation (Fig. 9.19). Cementite decomposition by that mechanism is clearly not occurring in the iron dusting reaction depicted in Figs. 9.17 and 9.18. Although the different gases react with the surface according to different mechanisms (see Section 9.6.3), it also seems that the direction of carbon transport is different in the two sorts of experiments.

The alternative mechanism of  $\text{Fe}_3\text{C}$  particle production is mechanical disintegration resulting from volume expansion [67,76]. Because  $\text{Fe}_3\text{C}$  is a carbon diffuser [77,78], the cementite layer grows inward and is consequently under compressive stress. Precipitation of graphite could occur at internal defects in a nucleation and growth process [67]. Such a process would be similar to the way carbon forms and grows at the rear of  $\text{Fe}_3\text{C}$  particles (Fig. 9.17). Growth of these precipitates could then disrupt the cementite surface. Examination of the  $\text{C}(\text{gr})/\text{Fe}_3\text{C}$  interface in Fig. 9.20 shows that graphite is growing into the cementite layer, and that nanoparticles of  $\text{Fe}_3\text{C}$  are detached from the bulk carbide. For these to exist, the carbon activity must be

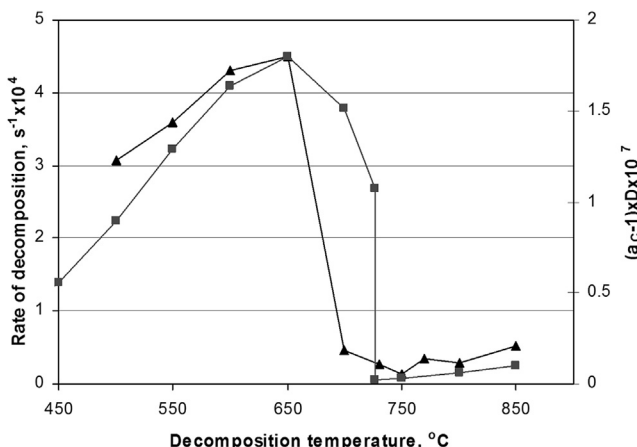


**FIGURE 9.19** Rate of  $\text{Fe}_3\text{C}$  decomposition measured ( $\blacktriangle$ ) in  $\text{H}_2/\text{CH}_4$  and calculated ( $\blacksquare$ ) from  $D_C$  and  $a_C$  in ferrite [73].

high enough to stabilise the phase. It is therefore concluded that the graphite layer does not function as a barrier to the gas, and that  $a_C$  at the coke-cementite interface is probably close to the value in the ambient gas.

This conclusion is supported by the observation [79] that the surface cementite layer continues to thicken, and that the carbon content of the iron specimen increases as dusting proceeds. It is clear that carbon is diffusing through the cementite scale and into the iron, and that the description of Fig. 9.18B applies. However, these experiments were of limited duration (up to c. 40 h) and at a single temperature. Once the iron sample reaches a steady state of carbon supersaturation, the mechanism may well change [80] when an inward flux of carbon is no longer possible. Moreover, it is likely that the

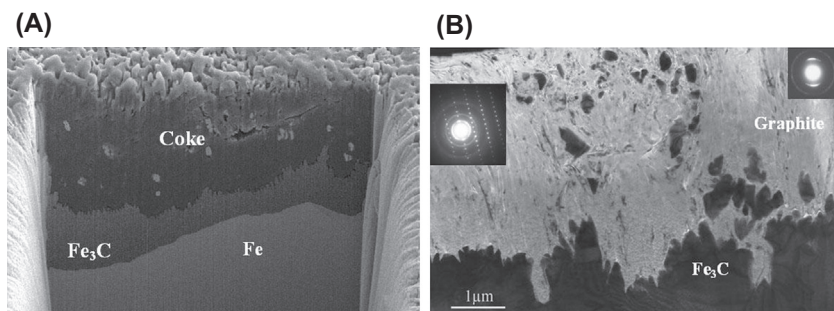


**FIGURE 9.20** Graphite-cementite interface developed during dusting of iron at 680°C: (A) FIB milled section and (B) TEM bright field with SAD identifying nanoparticles as  $\text{Fe}_3\text{C}$ . Reprinted from M.A.A. Motin, P.R. Munroe, M.P. Brady, D.J. Young, *Scripau Mater.* 56 (2007) 281 with permission from Elsevier.

mechanism changes with gas composition and temperature. Zhang et al. [69,81] have reported that at  $T = 700^\circ\text{C}$ , and low  $p_{\text{CO}}$  values, the surface  $\text{Fe}_3\text{C}$  scale decomposes to form a surface layer of ferrite. At still higher temperatures, no cementite layer is seen, and graphite deposits directly into the metal.

### 9.6.2 Iron Dusting in the Absence of Cementite

Given the important role played by cementite in the dusting of iron, it is reasonable to enquire whether dusting might be prevented if  $\text{Fe}_3\text{C}$  formation were suppressed. Cementite can be destabilised with respect to graphite by alloying with silicon to raise the solute carbon activity. Unfortunately, silicon also oxidises in the gases under discussion, as is discussed below. Germanium, on the other hand, forms a much less stable oxide, and by virtue of its chemical similarity to silicon, might be expected to suppress  $\text{Fe}_3\text{C}$  formation. This is indeed the case, as shown in Fig. 9.21, where graphite is seen to be growing directly into a ferritic Fe-Ge alloy, in the absence of any cementite. The nanoparticulate material near the disintegrating interface is also  $\alpha$ -(Fe,Ge), as are the particles found on coke filaments.

Alloying with germanium suppressed  $\text{Fe}_3\text{C}$  formation, but did not prevent metal dusting. Instead, dusting occurred more rapidly by the growth of graphite directly into the alloy. Metal particles were formed by disintegration of the bulk metal, as the graphite grew inwards. Again it is suggested that this was a consequence of the volume expansion accompanying nucleation and growth of graphite within the metal. This process was more rapid than the corresponding one involving  $\text{Fe}_3\text{C}$ . It is noteworthy that the Fe-Ge/graphite interface morphology is similar to that developed between nickel and graphite

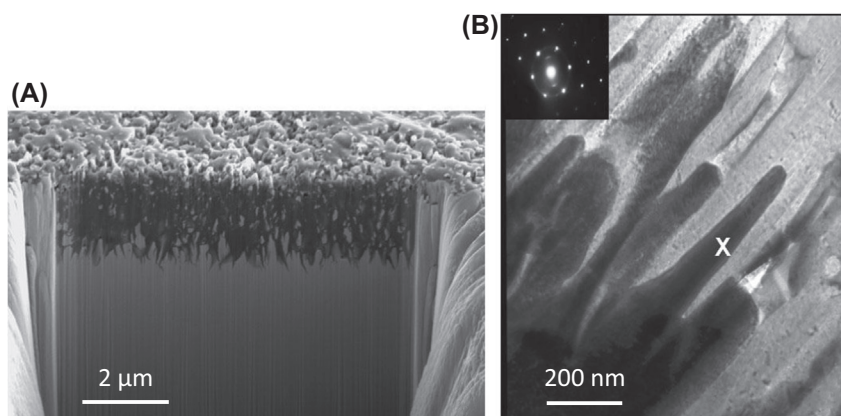


**FIGURE 9.21** Fe-10Ge alloy after 10 h reaction in  $\text{H}_2/\text{H}_2\text{O}/\text{CO}$  ( $a_{\text{C}} = 2.9$ ,  $p_{\text{O}_2} = 10^{-23}$  atm): (A) FIB cross-section and (B) TEM cross-section with SAD identifying  $\alpha$ -Fe. *Reprinted from M.A.A. Motin, P.R. Munroe, M.P. Brady, D.J. Young, Scripta Mater. 56 (2007) 281 with permission from Elsevier.*

(where no carbide forms) during dusting (see Section 9.7). However, dusting was much faster for the ferritic material. It is clear that suppression of  $\text{Fe}_3\text{C}$  formation does not prevent dusting when this alternative mechanism is available.

### 9.6.3 Effects of Temperature and Gas Composition on Iron Dusting

As noted by Grabke [82], iron dusting and coking kinetics are very complex, and more detailed studies are needed to arrive at a comprehensive, self-consistent picture. As seen in Fig. 9.22, somewhat different temperature dependencies have been reported for different gas conditions. Grabke et al. [61] considered the temperature dependence at  $T < 540^\circ\text{C}$  to reflect rate control by cementite decomposition, which they considered to be independent of gas composition. Ramarayanan et al. [65,83] identified two temperature regimes:  $T < 450^\circ\text{C}$  where the coke was amorphous and the rate was controlled by physical disintegration of  $\text{Fe}_3\text{C}$ , and  $450 < T < 570^\circ\text{C}$  where the chemical decomposition of  $\text{Fe}_3\text{C}$  was thought to become important. Its rate increased as the graphitisation of coke increased with temperature, providing a diffusion pathway for dissolved iron. The decline in dusting rates reported by Ramarayanan et al. at  $T > 570^\circ\text{C}$  was attributed by them to a decrease in  $a_{\text{C}}$  with increasing temperature. Grabke observed an increased dusting rate in the range  $540\text{--}620^\circ\text{C}$ , reporting it to vary with the product  $p_{\text{CO}}p_{\text{H}_2}$  [84], and concluded that carbon transfer from the gas was rate controlling.

Part of the reason for this confusion is the way in which  $a_{\text{C}}$  varies with temperature (Fig. 9.1) and gas composition (Eqs [9.10] and [9.11]) in  $\text{CO}/\text{H}_2/\text{H}_2\text{O}$  gas mixtures. The driving force for carbon precipitation ( $a_{\text{C}} - 1$ ) is

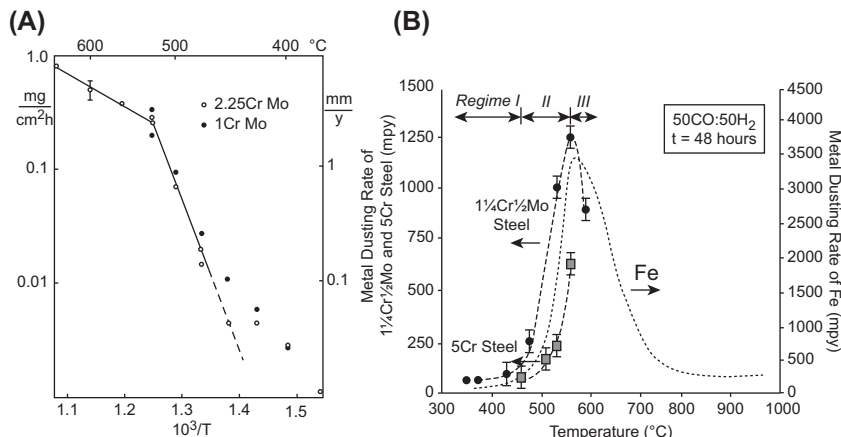


**FIGURE 9.22** Temperature effects on metal dusting for iron and low alloy steels (A) in  $\text{CO}/\text{H}_2/\text{H}_2\text{O}$  [84] and (B) in  $\text{CO}/\text{H}_2$  [83]. With kind permission from Springer Science and Business Media.

related to gas composition variables, which themselves appear in kinetic expressions. Distinguishing the two effects can be difficult and is impossible if the gas compositions are not carefully controlled. Thus the use of CO/H<sub>2</sub> gases without H<sub>2</sub>O to buffer the composition means that  $a_C$  is uncontrolled and will vary with the extent of carbon deposition. As carbon deposition rates are rapid around 550°C, both  $a_C$  and  $p_{CO}$  can vary considerably in a nominal CO-H<sub>2</sub> gas mixture, and the results of Fig. 9.22B are unreliable.

The dependence of both coking and dusting rates on the composition of CO/H<sub>2</sub>/H<sub>2</sub>O gases determined by Muller-Lorenz and Grabke [84] is shown in Fig. 9.23. Similar results were found for iron dusting at 550°C by Chun et al. [65]. In both cases it was concluded that the rate-determining step in the dusting process was Eq. [9.7], leading to

$$\text{Rate} = r_7 p_{CO} p_{H_2} \quad [9.38]$$

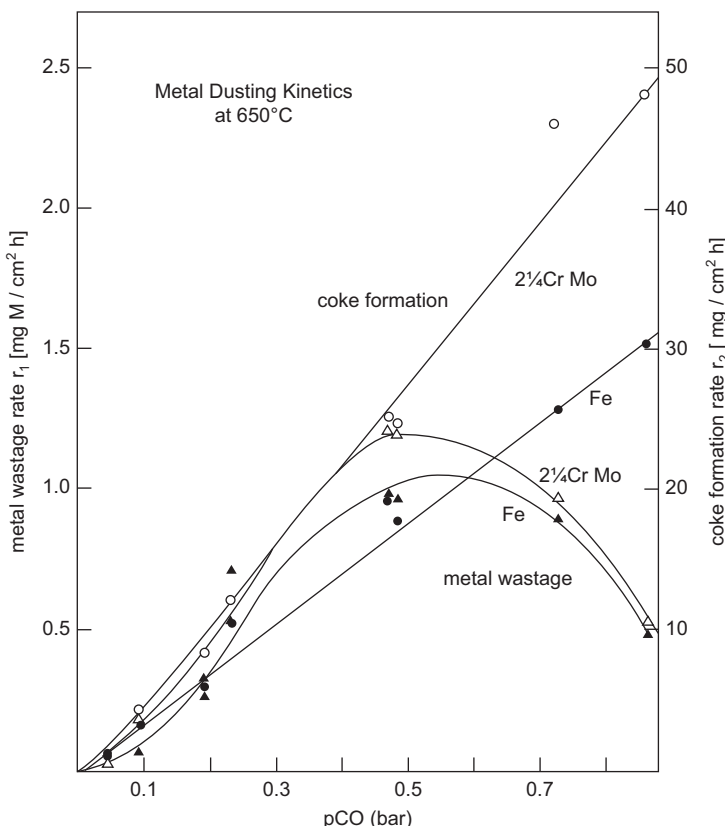


**FIGURE 9.23** Dependence of coking and dusting rates on  $p_{CO}$  in CO/H<sub>2</sub>/H<sub>2</sub>O mixtures [84]. Published with permission from Wiley-VCH.

However, this analysis neglects the effect of  $a_C$ . Experiments [85] in which  $a_C$  was maintained constant showed that keeping the product  $p_{CO}p_{H_2}$  constant but varying the individual partial pressures changed both coking and dusting rates. Obviously, the simple description of Eq. [9.38] cannot be applied to either process.

Considering the coking process first, it is seen that the Boudouard reaction (Eq. [9.8]) is likely to be important at high  $p_{CO}$  values. Furthermore, when  $p_{H_2}$  is high, it is likely that methanation (the reverse process in Eq. [9.9]) will occur under catalysed conditions. Ignoring the reverse reactions in Eqs [9.7] and [9.8] along with the forward process Eq. [9.9], we can write

$$\frac{d(\Delta W_C/A)}{dt} = r_7 p_{CO} p_{H_2} + r_8 p_{CO}^2 - r_{-9} p_{H_2}^2 \quad [9.39]$$

where the  $r_i$  are rate constants. As seen in Fig. 9.24, this expression is successful in describing coking rates with  $r_7 = 35.5$ ,  $r_8 = 4.5$  and  $r_{-9} = 5.6 \text{ mg cm}^{-2} \text{ atm}^{-2}$ . It is concluded that coke deposition can be described in terms of gas-solid kinetics involving parallel reaction pathways.

More information is required on the variation of dusting kinetics with gas composition. The available data for dusting in CO/H<sub>2</sub>/H<sub>2</sub>O mixtures at 500°C [86] and 650°C [87] indicate the rate increases with  $a_C$ . Data at 550°C [83] for wastage rates of iron exposed to CO/H<sub>2</sub> mixtures reveal a maximum at  $p_{CO} = 0.5 \text{ atm} = p_{H_2}$ . If the unavoidable water vapour impurity level was the same in all gases used, then  $a_C = K_7 p_{CO} p_{H_2} / p_{H_2O}$  also has its maximum at this composition.

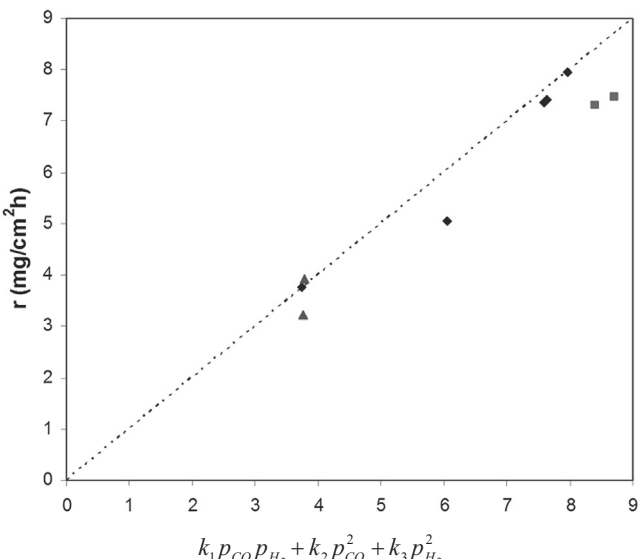


**FIGURE 9.24** Variation of coking rates on iron at 650°C according to Eq. [9.39] [85] with permission from Elsevier.

### 9.6.4 Dusting of Low Alloy Steels

Dusting of  $2\frac{1}{4}$  Cr-1Mo and  $1\text{Cr}-\frac{1}{2}\text{Mo}$  steels is seen in Figs 9.22 and 9.23 to be similar to pure iron in rate and dependence on temperature and gas composition. Reaction morphologies are also similar [82], and it may be concluded that mechanisms are the same. The reasons for the slightly faster dusting rates observed for  $2\frac{1}{4}$  Cr-1Mo steel have not been established. However, it is to be noted that in  $\text{CO}/\text{H}_2/\text{H}_2\text{O}$  gases, the  $p_{\text{O}_2}$  values are high enough to oxidise the chromium. Although no  $\text{Cr}_2\text{O}_3$  scales can form on such a dilute alloy, conversion of the steel surface to  $\text{Fe}_3\text{C}$  may lead to encapsulation of chromium-rich oxide particles. These might act as nuclei for graphite precipitates, thereby accelerating the cementite disintegration.

Addition of silicon to iron has two effects: a partial destabilisation of  $\text{Fe}_3\text{C}$  with respect to  $\text{C}(\text{gr})$  and the promotion of  $\text{SiO}_2$  formation at the oxygen potentials of  $\text{CO}/\text{H}_2/\text{H}_2\text{O}$  gases. At low alloy levels, the  $\text{SiO}_2$  forms as a dendritic internal precipitate rather than an external scale (Fig. 9.25). Thus the  $\text{SiO}_2$  provides little or no protection against carbon access to the metal. Cementite layers formed by Fe-Si alloys are thinner than on iron, coking is faster and metal wastage is also more rapid [79]. The internal  $\text{SiO}_2$  precipitates are incorporated into the  $\text{Fe}_3\text{C}$  scale as it grows into the alloy. These might act as graphite nucleation sites within the cementite, thereby accelerating its disintegration.

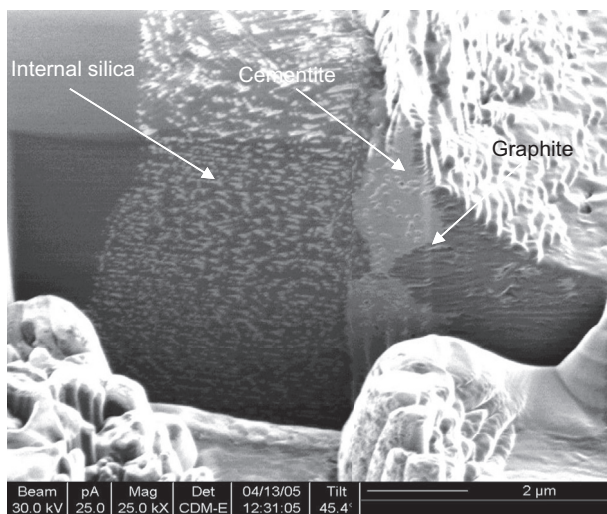


**FIGURE 9.25** FIB image of Fe-Si after dusting in  $\text{CO}/\text{H}_2/\text{H}_2\text{O}$  ( $a_c = 2.9$ ,  $p_{\text{O}_2} = 10^{-23}$  atm) at  $680^\circ\text{C}$ . Published from M.A.A. Motin, J. Zhang, D.J. Young, *J. Electrochem. Soc.* 157 (2010) C375 with permission from the Electrochemical Society.

### 9.6.5 Dusting of Ferritic Chromium Steels

The behaviour of these alloys when exposed to CO/H<sub>2</sub>/H<sub>2</sub>O gas mixtures depends on whether a chromia scale is formed and retained. If the alloy chromium level is too low to form a Cr<sub>2</sub>O<sub>3</sub> scale, the steel will dust at essentially the same rate as a 2½Cr-1Mo steel [87,88]. If the steel forms a continuous, adherent chromia scale, resistance to dusting under isothermal conditions is very good, because the scale is an effective barrier to carbon entry. The factors determining the success or otherwise of a steel in resisting dusting are those governing its ability to quickly form a continuous Cr<sub>2</sub>O<sub>3</sub> scale by diffusing chromium to the surface.

The effect of temperature on  $D_{\text{Cr}}$  is clear from the studies of Grabke et al. [60]. Steels containing 17 and 26 Cr showed complete resistance to dusting at 650 and 600°C but underwent a slight extent of attack at 550°C. Thus the susceptibility to dusting increased as the temperature and  $D_{\text{Cr}}$  decreased. The effective value of  $D_{\text{Cr}}$  can be increased at the low temperatures involved here by creating a deformed and fine-grained alloy surface. This is done by surface grinding, shot peening, etc., and has been shown [88] to lead to better dusting resistance. In the absence of such treatment (or after its effects have been annealed out) the ferritic nature of the alloy is itself important, because of the higher  $D_{\text{Cr}}$  value compared to austenitic materials. A comparison of the dusting performance of model ferritic and austenitic 25Cr alloys in Fig. 9.26 illustrates this point. These alloys had been electropolished to remove any cold-worked surface material, so that alloy chromium transport was via lattice diffusion.

Alloys which successfully develop continuous, protective chromia scales are nonetheless subject to long-term dusting attack. Under isothermal exposure conditions, growth stress accumulation in the scale leads ultimately to mechanical failure. A series of such events can exhaust the capacity of an alloy to regrow its protective scale, and metal dusting ensues [88,89]. Discontinuous exposures combine the effects of accumulated growth stress and occasional thermal expansions and contractions. These have also been shown to produce alloy depletion and eventual dusting [60,82,88,90]. Short-term thermal cycling experiments induce the same failure mode and are useful as accelerated corrosion tests [91]. In all cases, the chromia scale breaks down locally, allowing carbon to enter the chromium-depleted metal. Rapid inward diffusion of carbon leads to internal precipitation of chromium carbides, thereby preventing any subsequent rehealing of the scale. The depleted iron matrix forms a surface cementite layer [24,92] which disintegrates, producing numerous cementite particles which catalyse further coke deposition [24]. This localised attack produces a pitted surface (Fig. 9.27). However, as the reaction proceeds, more pits form, and they widen and coalesce until the attack becomes general.

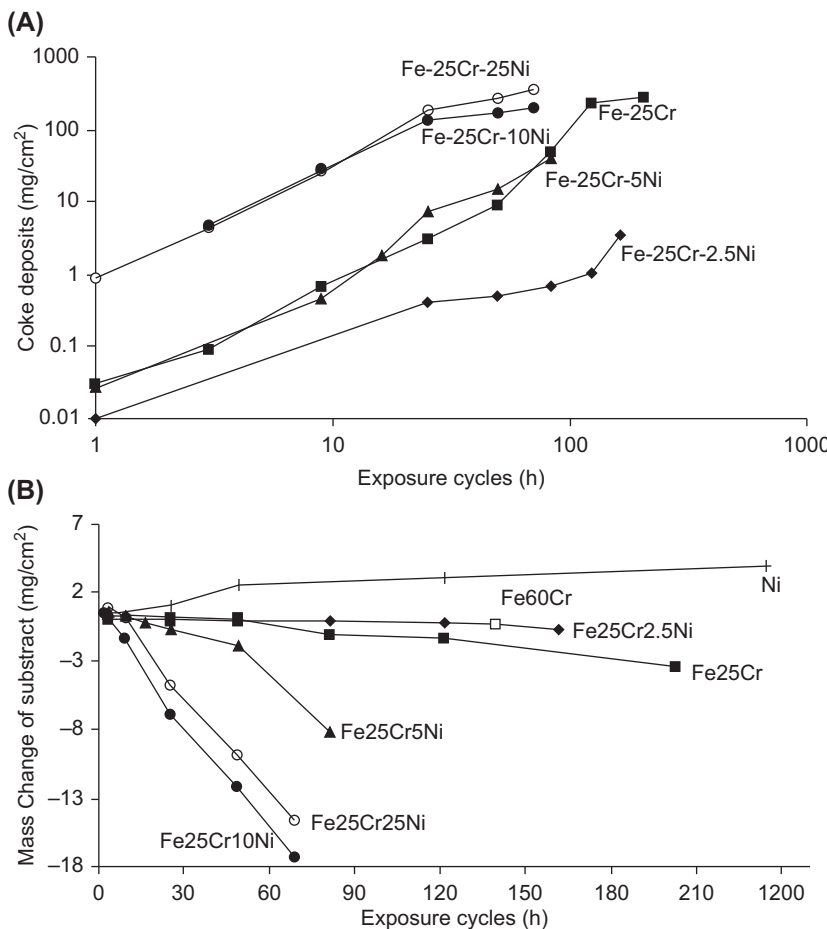


**FIGURE 9.26** Metal wastage kinetics for electropolished 25Cr alloys at 680°C in CO/H<sub>2</sub>/H<sub>2</sub>O ( $a_C = 2.9$ ,  $p_{O_2} = 10^{-23}$  atm) [24]. With kind permission from Springer Science and Business Media.

If the alloy chromium level is high enough, dusting of ferritics can be prevented. An Fe-60Cr alloy survived 1000 one-hour cycles at 680°C, forming only Cr<sub>2</sub>O<sub>3</sub> [24], which was impermeable to carbon. Furthermore, the chromia was catalytically inactive, and no coke deposited.

### 9.6.6 Dusting of FeAl and FeCrAl Alloys

Iron aluminides and FeCrAl alloys are able to develop alumina scales, and their ability to resist dusting is therefore of interest. The high diffusion coefficients

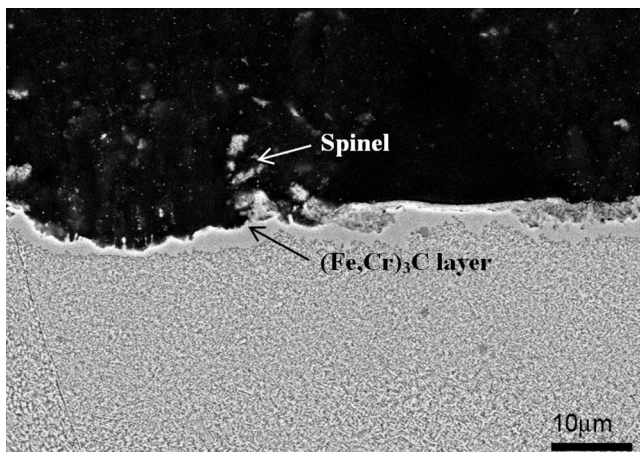


**FIGURE 9.27** Onset of dusting: Fe-25Cr reacted at 680°C in CO/H<sub>2</sub>/H<sub>2</sub>O ( $a_C = 2.9$ ,  $p_{O_2} = 10^{-23}$  atm) showing local internal carburisation, surface cementite layer and its disintegration.

characteristic of the ferritic FeCrAl materials (typically Fe-20Cr-5Al) means that they are able to reheat scales quickly, thereby preserving the surface barriers to carbon attack.

Dusting of the intermetallic Fe<sub>3</sub>Al at 650°C in CO-H<sub>2</sub>-H<sub>2</sub>O was investigated by Strauss et al. [93], who reported extensive attack at localised pits. After addition of 2.2% Cr to the alloy, dusting was confined to the unpolished specimen edges. With 4.8% Cr and 0.15% Zr, pitting was completely suppressed, and only a thin coke layer formed. Dusting was associated with formation of a surface layer of Fe<sub>3</sub>C. Further work on Fe-15Al and Fe-26Al by Schneider and Zhang [94,95] showed that dusting was also associated with internal precipitation of the  $\kappa$ -carbide, Fe<sub>3</sub>AlC<sub>x</sub>. Attack on Fe-15Al was general but was reduced to localised pitting by alloying with 2.9% of Nb or Ta, and almost stopped by adding 2% of either V or Ti. Increases in temperature or alloy aluminium content led to reduced dusting rates. As pointed out by the authors, the observations are consistent with protection against dusting due to Al<sub>2</sub>O<sub>3</sub> scale formation. However, at the relatively low temperature of 650°C, the binary intermetallic does not reliably form a continuous scale. Alloy additions of Cr, Nb, Ta, V and Ti all improve alumina scale formation. Nonetheless, once the scale is damaged, rapid carbon entry leads to internal carburisation of the alloy and prevents subsequent alumina re-healing. The mechanism is thus very similar to that of attack on ferritic Fe-Cr alloys.

The FeCrAl materials provide much better dusting resistance. Baker and Smith [90] reported that an oxide dispersion strengthened alloy, MA956, demonstrated very good dusting resistance at 621°C up to 9000 h in a CO-H<sub>2</sub>-H<sub>2</sub>O gas which was oxidising to aluminium. Good performance has also been reported [80,91] for FeCrAl materials at 650°C in similar

atmospheres. Internal precipitation of the  $\kappa$ -carbide was observed after several thousand hours [80], and filamentary coke growth was catalysed by  $\text{Fe}_3\text{C}$  particles [91] when the scale was damaged by repeated thermal cycling.

## 9.7 DUSTING OF NICKEL AND AUSTENITIC ALLOYS

Metal dusting of nickel and austenitic alloys differs from the reaction of ferritic materials in that cementite is not formed, and the corresponding nickel carbide is unstable. An examination of the dusting behaviour of pure nickel provides a good basis for understanding the reaction of austenitic, heat-resisting alloys.

### 9.7.1 Metal Dusting of Nickel

Exposure of nickel to carbon-rich gases at oxygen potentials where the metal does not oxidise leads to catalysis of Eqs [9.7–9.9], producing carbon. Hochman [56] and Schneider et al. [95] reported the rate of carbon uptake to be much slower than the corresponding process on iron. The kinetics are approximately linear [95,96] after an induction period of length varying with temperature and gas composition. Metal consumption kinetics have not been measured directly. It is usually assumed that the carbon deposit contains an approximately constant nickel concentration (1–2 wt.%), and on this basis, linear dusting kinetics would be deduced. Chun et al. [97] measured metal surface recession after a seven-hour reaction in an unbuffered gas mixture of CO and  $\text{H}_2$  in the proportions 25:1 and found average rates to be of order 1 mm/year at temperatures above 600°C.

Reaction morphologies vary with ambient conditions, and the available information is incomplete. The 25:1 CO/ $\text{H}_2$  gas produced external attack, whereas at a CO to  $\text{H}_2$  ratio of 1:1, extensive internal graphitisation also resulted. The appearance of both forms of attack on coarse-grained nickel exposed to a CO/ $\text{H}_2/\text{H}_2\text{O}$  gas is shown in Fig. 9.28. Cold working the metal surface prior to the reaction induced recrystallisation of the near-surface region and graphite formation at the multiple grain and sub-grain boundaries. It is clear that carbon dissolves in the nickel and diffuses inwards, supersaturating the metal until graphite precipitates nucleate and grow at favourable sites. Nava Paz and Grabke [58] reported earlier that CO/ $\text{H}_2/\text{H}_2\text{O}$  mixtures with low  $p_{\text{CO}}$  led to internal graphitisation, whereas high  $p_{\text{CO}}$  mixtures induced surface deposition.

Coke accumulates on the external nickel surface in three forms: a more-or-less uniform layer adjacent to the surface, clusters of approximately spherical particles, and filaments (Fig. 9.29). The carbon spheres contain nickel particles and the filaments carry nickel particles at their tips. The presumed correlation between coke mass and metal consumption is seen to be reasonable. Nickel is



**FIGURE 9.28** Graphitisation of nickel exposed to  $\text{CO}/\text{H}_2/\text{H}_2\text{O}$  ( $a_{\text{C}} = 19$ ) for 100 h at  $650^{\circ}\text{C}$ . Reprinted from J. Zhang, D.J. Young, Corros. Sci. 49 (2007) 1496 with permission from Elsevier.

catalytically active to all of Eqs [9.7–9.9], and it was proposed long ago [72] that reactions such as



where  $\underline{\text{C}}$  represents carbon dissolved in nickel, occur on the bare facets of the nickel particles. The carbon then diffuses rapidly through the particle and precipitates at the rear faces, causing elongation of the carbon filament. If the exposed nickel faces cannot dissolve carbon quickly enough, the particle is encapsulated with graphite, forming a roughly spherical particle like those in Fig. 9.29. The accumulation of the outer, loose coke deposit is thereby explained. Of more interest, however, is the development of coke at the metal surface, and the way in which parent metal is ‘dusted’ to form the catalytic nanoparticles.

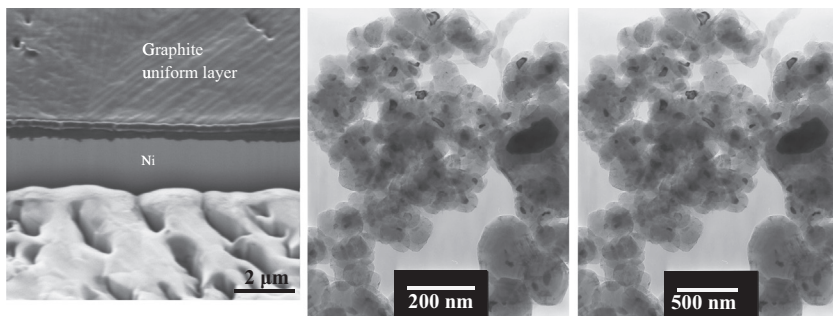


**FIGURE 9.29** Coke developed on nickel exposed to  $\text{CO}/\text{H}_2/\text{H}_2\text{O}$  ( $a_{\text{C}} = 19$ ) at  $650^{\circ}\text{C}$ : uniform layer, particle clusters and filaments.

Zeng and Natesan [98] used Raman spectroscopy, which is sensitive to the degree of carbon crystallinity, to show that the surface carbon layer was more graphitic than the outer coke. Grabke et al. [95,99], Pippel et al. [64,100] and Chun et al. [97] all used transmission electron microscopy to examine the nickel–carbon interface. These authors agreed that the carbon was graphite, that the graphite basal planes were oriented approximately normal to the nickel surface when dusting occurred and that nickel was dissolved (1–2 wt.%) in the graphite. The mechanism deduced from these observations was one of outward diffusion of solute nickel through the graphite, followed by precipitation of nickel particles in the outer regions of the graphite layer. The fundamental difficulty with this mechanism is essentially the same as was identified earlier in the iron dusting case. No driving force is apparent for mass transfer from bulk nickel to particulate metal, which would presumably be at a higher energy level as a result of its large specific surface area.

A TEM image of the graphite layer and nickel concentrations analysed within it by EDS [101] are shown in Fig. 9.30. Little or no concentration gradient is apparent, suggesting either that no diffusion occurs or that  $D_{Ni}$  in graphite is extremely high. Examination of the microstructure in Fig. 9.30 shows that in fact nickel nanoparticles are distributed throughout the graphite layers. Thus the surface layer is a two-phase, two-component material in which isothermal diffusion could not occur if local equilibrium was in effect. It

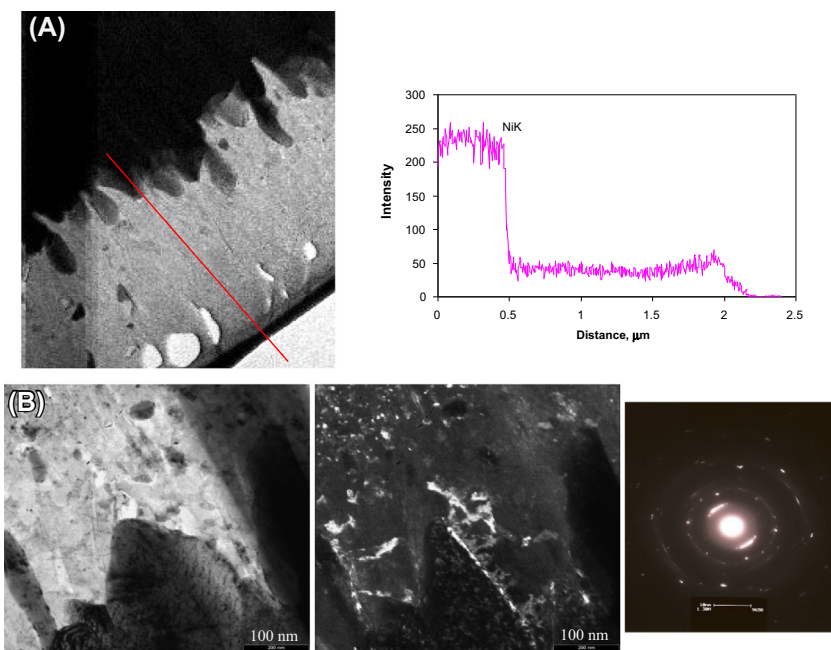


**FIGURE 9.30** (A) TEM bright field view and EDS line scan through uniform graphite layer on nickel and (B) bright and dark field images using (111) nickel reflection reveal particulate metal in graphite ( $\text{CO}/\text{H}_2/\text{H}_2\text{O}$ ,  $a_{\text{C}} = 19$ ,  $T = 680^\circ\text{C}$ ) [101].

is nonetheless possible that a single-phase graphite-nickel solution might form under other reaction conditions, and the nickel diffusion model could apply. In the example shown, it appears that mechanical disintegration of the metal is a consequence of the inward growth of graphite and the accompanying volume expansion. Such a process was in fact deduced from the original electron microscopy studies [64,96,98,100], and the proposed diffusion of nickel through graphite is of secondary importance.

The mechanism of graphite nucleation and growth is of fundamental importance to the dusting process. It is proposed [96,98,101] that the free edges of graphite basal planes act as attachment sites for carbon atoms, permitting their extension into the metal (Fig. 9.31A). The supply of carbon necessary for this process can only be maintained if direct gas access to the base metal continues throughout the reaction. Even when the surface is covered with graphite and coke, no effective barrier to the gas is formed. Most of the coke is obviously porous, and even the more dense graphite layer is extensively fissured.

The factors controlling graphite formation on nickel have been investigated intensively because carbon fouling (coking) of industrial nickel catalysts is an important practical problem. Direct surface observation [103] using low energy election diffraction (LEED) showed that a preferred epitaxial relationship developed between the graphite basal plane (0001) and Ni (111) faces. A computer simulation of this arrangement is shown in Fig. 9.31B. Electron diffraction studies [104] confirmed that (111), (113) and (220) nickel faces were found at carbon filament-metal interfaces. The same epitaxies are observed in metal dusting studies.

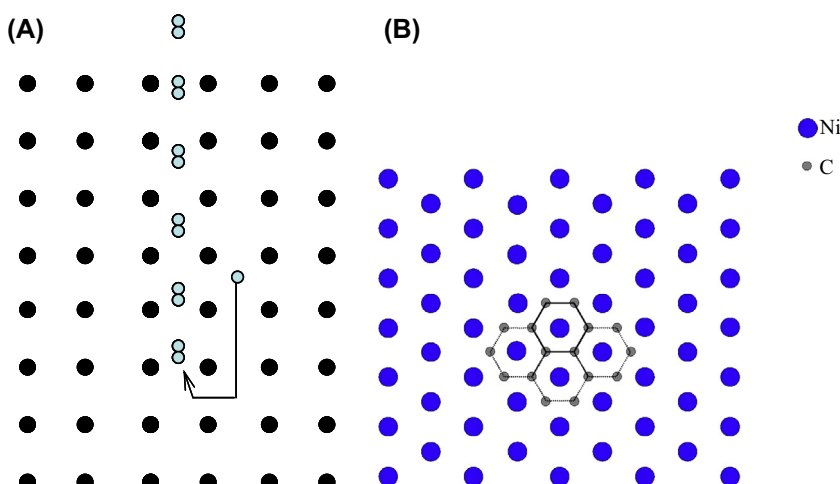


**FIGURE 9.31** (A) Schematic view of graphite growth into nickel. (B) Computer simulation of the epitaxial relationship between the graphite basal plane and a Ni (111) plane.

Examination by TEM of reacted nickel single crystal and polycrystalline surfaces [64,98,100] revealed that graphite basal planes developed parallel to nickel (111) and (110) surfaces, but at right angles to a (100) surface. In the short-term, no dusting occurred at the (111) or (110) surfaces, but on the (100) surface, graphite grew into the nickel, causing its disintegration. This pattern of behaviour is clearly consistent with the reaction model of Fig. 9.31, which requires the graphite basal planes to be oriented at an angle to the surface. Of course, the description is somewhat oversimplified. Consider, for example, a (111) surface which is in fact intersected by planes such as (11 $\bar{1}$ ), providing favourable inward growth directions for graphite. These will be accessible at surface jogs, kinks, etc., and dusting does in fact ultimately commence on these surfaces [64,98,100].

Graphite growth into the metal along nickel (111) and (113) planes is shown in Fig. 9.32. Penetration of graphite basal planes between adjacent planes of the nickel lattice destroys its structure. It has been suggested [99,101] that the graphite nucleates within the metal interior, and this is self-evidently the case for internal graphitisation (Fig. 9.28). Such a process is analogous to the dissolution-precipitation mechanism producing carbon filaments from nickel nanoparticles. Some insight into the process can be gained from a consideration of alloying effects.

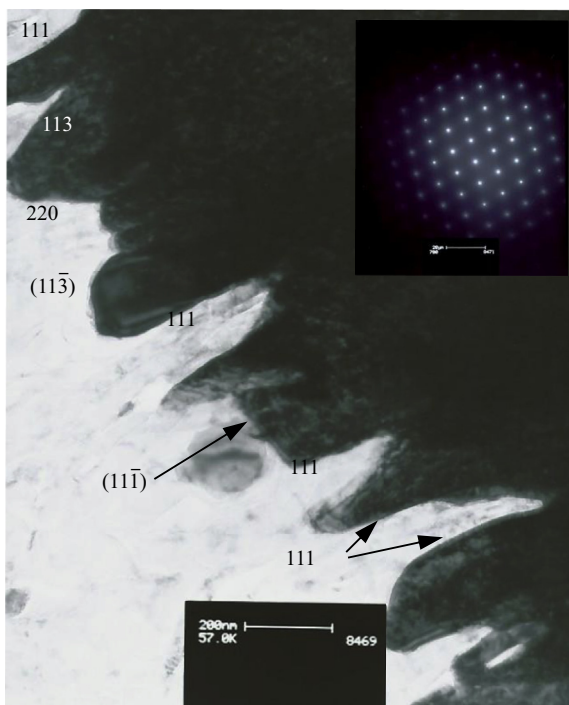


**FIGURE 9.32** Nickel facets at graphite-metal reaction front determined by SAD. Reprinted from J. Zhang, D.J. Young, *Acta Mater.* 56 (2008) 68 with permission from Elsevier.

### 9.7.2 Dusting of Nickel Alloys in the Absence of Oxide Scales

The dusting of austenitic Ni-Fe alloys at 650°C in CO/H<sub>2</sub>/H<sub>2</sub>O gases such that no oxidation occurred was studied by Grabke et al. [106], who found that both coking and metal wastage rates increased monotonically with iron concentration. The changes in coking rate reflected a combination of changing catalytic activity and dust particle size. Regardless of alloy iron content within the range 0–70%, the reaction morphologies were the same as for pure nickel. The dependence of dusting rate on alloy composition can be understood in part from the carbon permeability data of Fig. 9.12. The higher permeability of iron-rich alloys would provide a greater flux to the graphite nucleation and growth sites, supporting more rapid graphitisation and metal dusting.

More recent studies of Ni-Fe alloy dusting [107] have extended the range of alloy compositions and have confirmed the role of carbon permeation in the alloy. The kinetics of carbon uptake were at first parabolic, subsequently becoming linear. Carbon was produced in two forms: relatively dense material growing into the metal and nanotubes or filaments extending out into the gas, yielding the reaction morphology shown in Fig. 9.33. Diffusion control of the rate at which the surface coke depth,  $L$ , increases leads initially to

$$\frac{dL}{dt} = J_C \quad [9.41]$$

where the carbon flux,  $J_C$ , is evaluated from a simple steady-state description:

$$J_C = \frac{D_C}{L} \left( N_C^{ss} - N_C^{(s)} \right) \quad [9.42]$$

Here  $N_C^{ss}$  is the supersaturated carbon concentration produced at the metal-reaction gas interface, and  $N_C^{(s)}$  the concentration in equilibrium with graphite, the conventionally defined solubility. If, furthermore, the mass fraction of carbon within the surface layer is constant, the observed parabolic weight uptake kinetics are accounted for. This stage ends when disintegration of the layer at its outer surface becomes important. If the latter process occurs at a constant rate,  $k_d$ , then

$$\frac{dL}{dt} = \frac{k_p}{L} - k_d \quad [9.43]$$

and a constant value of  $L$  is arrived at. Using the definition  $a_C = \gamma_C N_C$ , and assuming a constant value for  $\gamma_C$ , one finds from Eq. [9.42]

$$J_C = \frac{D_C}{L\gamma_C} (a_C - 1) \quad [9.44]$$

In the experiments on Ni-Fe dusting [107], the gas composition and temperature were fixed. Therefore  $a_C$  was constant, and the effect of alloy composition on rate is attributable to variation in  $D_C$  and  $\gamma_C$ .

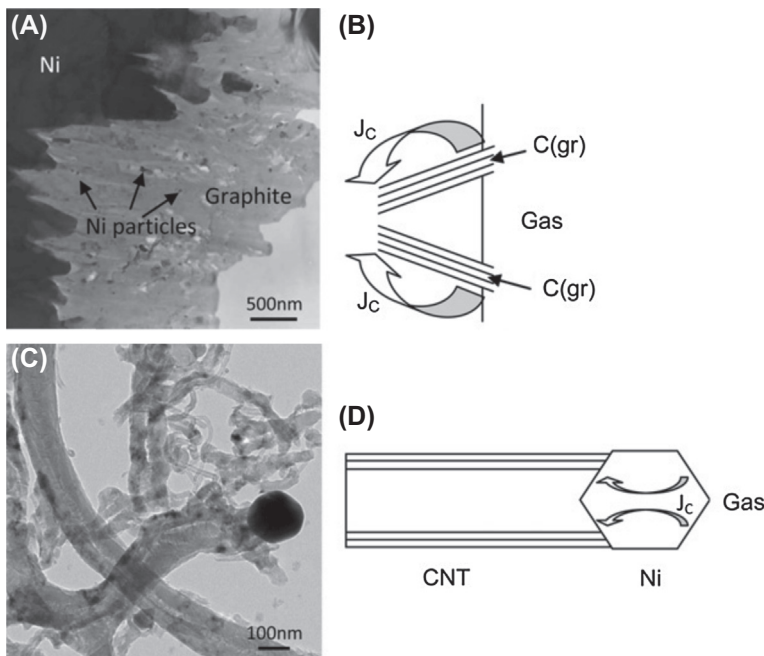


**FIGURE 9.33** Reaction morphology and mass transfer mechanisms in the metal dusting of nickel: (A, B) graphite growing into bulk metal and (C, D) multiwalled carbon nanotube growing from nanoparticle. *Reprinted from J. Zhang, D.J. Young, Corros. Sci. 56 (2012) 184 with permission from Elsevier.*

It follows from the definition of  $N_C^{(s)}$  that

$$\gamma_C = \frac{1}{N_C^{(s)}} \quad [9.45]$$

and therefore

$$J_C = \text{const. } D_C N_C^{(s)} \quad [9.46]$$

for the steady-state situation where  $L$  is constant. Dust particles had the same composition as the parent alloy, so combination of this carbon flux with appropriate geometric factors for both the bulk alloy and nanoparticle surfaces yields the overall coking rate. The relative magnitudes of the active surfaces of bulk alloy and particles were not measured, but the variation of  $J_C$  with alloy composition can be investigated. Values of  $D_C$  [20] and  $N_C^{(s)}$  [3] in Fe-Ni alloys at high temperatures were extrapolated to 650°C and their product, carbon permeability, is plotted as a function of binary alloy composition in Fig. 9.34. Measured linear rate constants for carbon uptake are also plotted in this figure, showing that the alloy composition dependence of

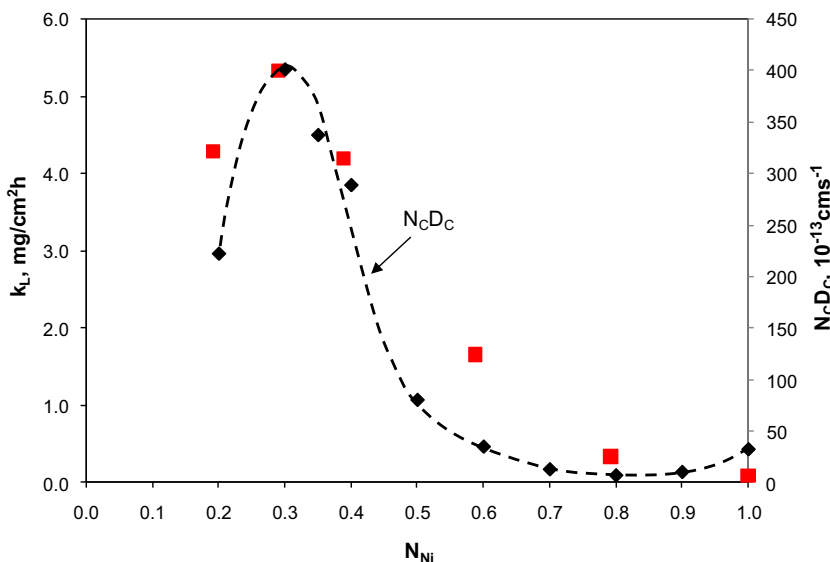


**FIGURE 9.34** Measured coking rates ( $k_L$ ) compared with  $N_c D_c$  as function of  $N_{Ni}$  for Ni-Fe alloys at  $650^\circ\text{C}$  in  $\text{CO-31\%H}_2\text{-1\%H}_2\text{O}$  ( $a_C = 33$ ,  $p_{O_2} = 7 \times 10^{-26}$  atm). Reprinted from J. Zhang, D.J. Young, Corros. Sci. 56 (2012) 184 with permission from Elsevier.

carbon uptake rate follows that of the permeability, in agreement with Eq. [9.46]. In particular, the unusual dependence of the rate on alloy composition in the 20–40 wt% Ni range is well-predicted by the permeability data. On this basis, however, pure nickel would be predicted to dust more rapidly than alloys with ~80% Ni, but in fact the metal dusted more slowly than the alloy. More information is required for high Ni/Fe ratios, which are typical of Inconel alloys.

Essentially the same diffusion model was applied earlier [108] to carbon transfer through a nickel nanoparticle from a facet in contact with gas to one from which a carbon filament was growing (Fig. 9.33). Using measured particle size to obtain  $L$  and independently measured values of  $D_C$  and  $\gamma_C$ , the rate of carbon delivery was calculated, and a carbon filament growth rate of  $1.5 \text{ nm s}^{-1}$  thereby predicted. Good agreement with measured average filament growth rates of  $\sim 3 \text{ nm s}^{-1}$  provides additional support for the model of Fig. 9.33 and Eq. [9.42].

Alloying copper with nickel has been found [105,109] to decrease coking and dusting rates sharply (Fig. 9.35). The coke deposit on alloys containing at least 10 wt% copper consisted solely of filaments. Thus metal wastage via the process leading to graphite particle clusters (Fig. 9.29) was suppressed. Copper is known to be immune to dusting attack, but its effect on nickel alloy dusting was much greater than one of simple dilution. Similar results have

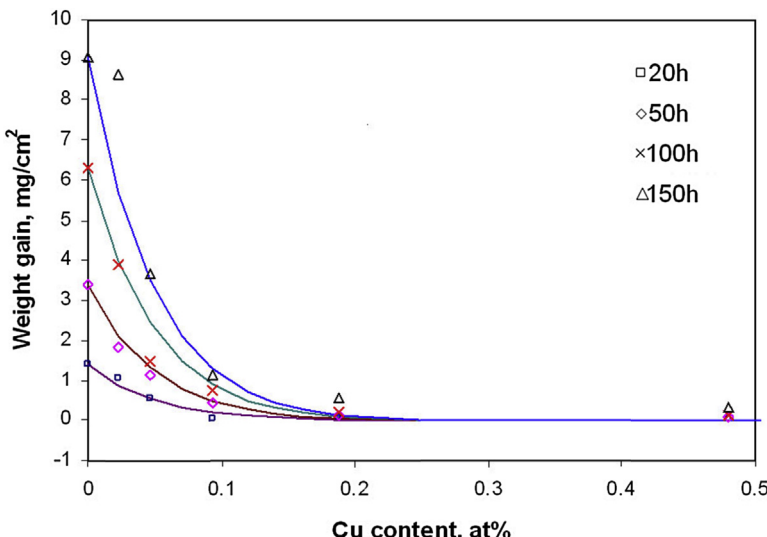


**FIGURE 9.35** Carbon uptake on Ni-Cu alloys at 680°C in CO/H<sub>2</sub>/H<sub>2</sub>O ( $a_{\text{C}} = 19$ ). Continuous lines calculated from Eq. [9.47] [105]. Published with permission from Wiley-VCH.

been reported [110–112] for the effect of copper on catalytic coking by nickel. This can be understood [110,112,113] if the catalytically active sites consist of  $y$  near-neighbour atoms. Then the carbon deposition rate on an alloy,  $r$ , is described by

$$r = r_{\text{Ni}}(1 - N_{\text{Cu}})^y \quad [9.47]$$

where  $r_{\text{Ni}}$  is the rate on pure nickel. The effect of copper can be described by this equation with  $y = 18$ , as shown by the calculated lines in Fig. 9.33.

A catalytic site of 18 near-neighbour atoms is physically unrealistic if surface reactions of simple molecules (eg, Eq. [9.40]) are involved. However, if graphite nucleation is the process being catalysed, then a stable nucleus presumably requires at least one hexagonal carbon ring. As seen in Fig. 9.31, it would require seven near-neighbour nickel atoms on a free surface or 14 atoms on adjacent (111) planes for internal nucleation. It is therefore concluded that the copper effect is consistent with internal graphite nucleation.

Copper alloying could also affect carbon solubility in the metal. The solubility is reported by one source [114] to be reduced from a maximum of 0.18% in nickel to about 0.01% in Ni-90Cu. However, Mckellan and Chrashka [115] showed that carbon solubility was unaffected by the presence of up to 40% copper. This conflict has been resolved by experiments [116] on the internal carburisation of Ni-Cr and Ni-Cu-Cr alloys at  $a_{\text{C}} = 1$ , which showed that values of  $k_p^{(i)}$  for chromium carbide precipitation were unaffected by the presence of copper at the levels of 5–20 wt% tested. It follows from Eq. [9.24]

that alloyed copper does not affect carbon permeability,  $N_{\text{C}}D_{\text{C}}$ , and it is concluded that the effect of copper in reducing nickel dusting is indeed one of inhibiting graphite nucleation. Alterations in electron band structure resulting from copper additions have also been suggested [117] to affect catalysis of carbon release from the gas.

Additions of copper have also been shown [107] to reduce dusting rates for Ni-Fe alloys containing up to 70 atom % iron. Eq. [9.47] was found to describe the effect, with  $r_{\text{Ni}}$  replaced by  $r_{\text{Ni-Fe}}$ , the rate observed for the copper-free binary alloy. Thus the effect of copper is apparently general for austenitic alloys. This effect can be included within the carbon permeation model of Eq. [9.42] by recognising the thermodynamic consequences of making graphite nucleation more difficult. In the presence of alloyed copper, a higher degree of carbon supersaturation is required to precipitate graphite. Thus a higher value of  $N_{\text{C}}^{(\text{s})}$  will be in effect, thereby decreasing the inward flux of carbon and slowing the reaction.

### 9.7.3 Effects of Temperature and Gas Composition on Nickel Dusting

Average metal recession rates in a 50-50 mixture of CO-H<sub>2</sub> were found [98] to increase with temperature to a maximum at about 800°C and to remain constant at higher temperatures. The carbon activity in those experiments was uncontrolled, and interpretation of the high temperature results is therefore difficult. The low temperature results were correlated with an observed increase in carbon graphitisation with increasing temperature. Chun et al. [98] suggested that dusting was controlled by outward diffusion of nickel dissolved in graphite, and therefore accelerated with increased graphitisation of the coke. However, it could also be argued that only graphite, and not amorphous carbon, was capable of growing into the metal, because graphite can develop a crystallographic orientation relationship with the metal. Increasing graphitisation would therefore increase the extent of nickel disintegration. Carbon uptake rates in a gas mixture of H<sub>2</sub>-24CO-2H<sub>2</sub>O were found by Schneider et al. [96] to have a maximum at about 625°C, and decreased sharply at higher temperatures, reflecting the lower carbon activities reached at higher temperatures in a gas of fixed composition.

Direct measurements of the dependence of metal consumption (ie, dusting) rates on gas composition are lacking, but data are available for coking rates. At a fixed temperature of 650°C, carbon uptake rates vary with gas composition in a complex way. Experiments in which  $p_{\text{CO}}$  and  $a_{\text{C}}$  (as calculated from Eq. [9.10]) were varied independently [97] showed that carbon uptake rates were not directly related to  $a_{\text{C}}$ . Using instead an elementary kinetic description for Eqs [9.7–9.9], one arrives at Eq. [9.38]. The success of this description is demonstrated in Fig. 9.36, with  $r_7 = 0.73$ ,  $r_8 = 0.06$  and  $r_{-9} = 0.27 \text{ mg cm}^{-2} \text{ atm}^{-2} \text{ h}^{-1}$ . This indicates that coke formation is controlled by the CO + H<sub>2</sub>

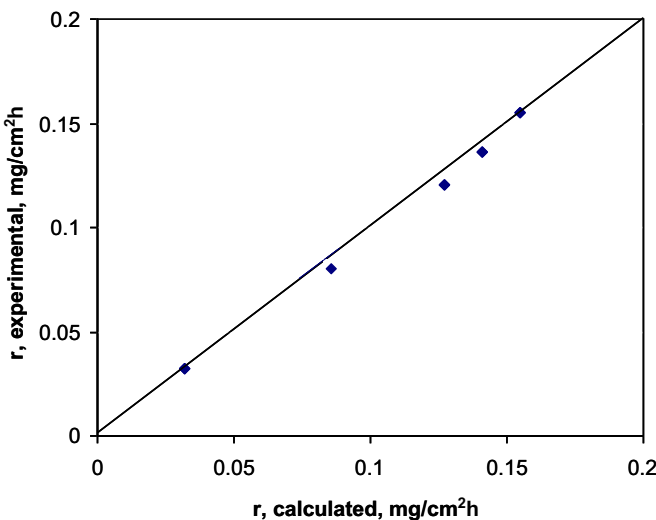


**FIGURE 9.36** Carbon uptake rates on nickel in CO/H<sub>2</sub>/H<sub>2</sub>O at 650°C, plotted according to Eq. [9.39]. Reprinted from J. Zhang, D.J. Young, *Corros. Sci.* 49 (2007) 1496 with permission from Elsevier.

reaction (Eq. [9.7]) at moderate  $p_{\text{CO}}$  levels and by the Boudouard reaction (Eq. [9.8]) at high  $p_{\text{CO}}$  levels. The methanation process is important when  $p_{\text{H}_2}$  is significant. It needs to be recognised that different dependencies are likely at different temperatures, and that the relationship between coking and dusting rates is likely also to be temperature-dependent. More work is required to obtain a full understanding of the effects of environmental variables on nickel dusting.

#### 9.7.4 Dusting of Austenitic Alloys

Grabke et al. [102,106] found that the dusting of binary Fe-Ni alloys varied in reaction morphology and rate with nickel content. Essentially, low nickel content alloys behaved like pure iron, forming a surface layer of cementite, whereas high nickel alloys graphitised directly without forming carbide. The nickel level necessary to suppress cementite formation at 650°C has been reported as 30% [106] and also [102] as 5–10%.

The dusting of austenitic chromia-forming alloys is prevented for so long as the oxide scale acts a barrier to carbon ingress [56]. The onset of dusting has been characterised by Grabke and co-workers [58,60,106], and the general features of the process are now clear. Selective oxidation of chromium produces a Cr<sub>2</sub>O<sub>3</sub> scale and a chromium-depleted subsurface alloy region, until local scale damage allows gas access to the metal. If sufficient chromium remains, the Cr<sub>2</sub>O<sub>3</sub> scale re-heals; if not, other reactions follow. In the usual case,  $p_{\text{O}_2}$  is too low for nickel or iron oxides to form, and instead, carbon enters the alloy, precipitating chromium carbides. At these low temperatures,

$D_{Cr}$  in the alloy is small, and the carbides are consequently very fine. Removal of chromium from the matrix renders future oxide healing of the surface impossible, and gas access to the chromium-depleted surface continues. The surface is now essentially an Fe-Ni alloy, and at high nickel levels, it undergoes graphitisation and disintegration in the same way as pure nickel.

Thermal cycling dusting studies [24] on model Fe- $x$ Ni-25Cr alloys revealed considerable variation in metal wastage rate with nickel content (Fig. 9.26). A 2.5Ni alloy was ferritic, and formed a surface layer of  $M_3C$ , which disintegrated into cementite dust. Alloys with 5 and 10Ni had duplex  $\alpha + \gamma$  microstructures, in which the austenite was clearly carburised more rapidly than the ferrite. Dusting produced nanoparticles of  $M_3C$  from the 5Ni alloys and both  $M_3C$  and austenite from the 10Ni alloy. A 25Ni alloy was fully austenite and disintegrated to yield austenite dust. This shift from carbide to austenite particles with increasing nickel levels is the same as that seen for binary Fe-Ni alloys [102,106] and reflects the mechanism of attack on chromium-depleted surfaces.

The variation of dusting rate with Fe/Ni ratio shown in Fig. 9.26 reflects mainly the difference in  $D_{Cr}$  accompanying the change from ferritic to austenitic structures. Because the alloy surfaces were electropolished and any cold-worked surface regions removed, chromium was available to the surface only via lattice diffusion. Thus rehealing was more effective, and frequency of dusting initiation less, in the alloy sequence  $\alpha > (\alpha + \gamma) > \gamma$ . At still higher nickel levels, improved performance resulted from the lowering of alloy carbon permeability (Section 9.7.2).

A growing body of results on the dusting resistance of austenitic alloys is becoming available. It is generally agreed [60,90,106,118] that higher nickel levels are beneficial, and that a minimum chromium level of about 25% is required [118,119]. At these levels, scale breakdown allows formation of two internal carbide zones, usually spheroidal  $M_7C_3$  near the surface and lamellar or Widmanstatten  $M_{23}C_6$  at greater depths [24,120]. Alloy additions of silicon and aluminium improve the ability of the scale system to exclude carbon [59,90,121–123]. Additions of carbide-forming metals (Mo, W, Nb) form stable carbides. Their ability to getter carbon allows unreacted chromium to reheat the surface scale, delaying the onset of dusting [123]. However, subsequent oxidation of these refractory metal carbides leads to volume expansion and disruption of the protective scale [124]. It has been shown [125] that additions of copper improve the dusting resistance of 310 stainless steel and alloy 800, just as copper decreases the dusting of nickel itself. This effect is limited by the alloy solubility for copper, which increases with nickel concentration.

Szakalos et al. [25,80,126] have pointed out that the fine internal carbides formed after scale failure can be oxidised in situ, leading to disruption of the metal and contributing to the dusting process. This phenomenon is illustrated in Fig. 6.38, and is in fact the ‘green rot’ corrosion process [127], in which the

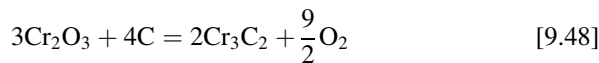
large volume expansion accompanying carbide oxidation fractures the metal. Under dusting conditions, this could occur simultaneously with graphitisation of the chromium-depleted surface metal. The two possible reactions for internal carbides near the surface are the oxidation process and simple dissolution, providing a chromium diffusion flux toward the surface. The competition between the two processes will depend on oxygen and carbon permeabilities and  $D_{Cr}$  within the subsurface alloy region. Rates of carbon and oxygen dissolution into the region are likely to depend also on gas compositions.

## 9.8 PROTECTION BY OXIDE SCALING

As noted earlier, industrial gas streams which cause carburisation are almost always oxidising to chromium, and therefore also to silicon and aluminium. Heat-resisting alloys used at temperatures up to about 1000°C are usually chromia formers, and the protective nature of their scales is what preserves the alloys from carburisation. Using radioactive  $^{14}C$ , Wolf and Grabke [128] showed that the solubility of carbon in  $Cr_2O_3$  and  $Al_2O_3$  at 1000°C is below the detectability limit of 0.01 ppmm. Nonetheless, chromia scales grown on alloy surfaces can be permeable to carbon, presumably by transport through defects or along internal surfaces. Grabke et al. [129] showed that radiotracer carbon in a  $CO/CO_2/H_2/H_2O$  gas mixture slowly permeated scales on pre-oxidised Fe-Cr alloys. Simultaneous internal carburisation and external  $Cr_2O_3$  growth have been observed [130] on Fe-28Cr exposed to  $CO/CO_2$  at 900°C. However, a Ni-28Cr alloy reacted in the same way formed no internal carbides, indicating a more gas tight scale.

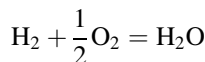
Cast heat-resisting steels form scales consisting of mixed carbides and oxides, the proportion of oxide increasing with ambient  $p_{O_2}$ . At high-oxygen activities, the scale is mainly  $Cr_2O_3$  with an outermost layer of manganese-rich spinel and, depending on alloy silicon levels, a more or less continuous  $SiO_2$  layer at the alloy-scale interface. For so long as they maintain their mechanical integrity, these scales completely block carbon access to the underlying alloys. The appearance of scales grown at 1000°C, low  $p_{O_2}$  values and  $a_C = 1$  and the corresponding diffusion paths mapped on the thermochemical diagram are shown in Fig. 9.37. The scale grown at  $p_{O_2} = 10^{-22}$  atm is a mixture of oxide (dark) and carbide (light) with a sublayer of  $SiO_2$  (black). The protectiveness of these scales depends on alloy silicon content, as shown in Fig. 9.38, where a level of about 1.8 w/o is seen to reduce the carburisation rate dramatically at 1050°C. Kane [29] reported a value of 2 w/o to be required at 1093°C. At  $p_{O_2} = 10^{-24}$  atm,  $Cr_2O_3$  is unstable, but  $SiO_2$  still forms. Exposure to these conditions [131] led to a scale of carbide over a thin silica layer at the alloy surface. This scale was not protective, and alloys carburised rapidly, even at silicon levels up to 2.4 w/o. It is therefore concluded that conditions producing both  $SiO_2$  and  $Cr_2O_3$  are necessary to provide a carbon-resistant scale.

The location of the stability boundary between chromium carbide and oxide shown in Fig. 9.37C is temperature-dependent:



$$\Delta G^\circ = 3,192,100 - 797.3T (\text{J mol}^{-1}) \quad [9.49]$$

In the presence of a coke deposit,  $a_{\text{C}} = 1$ , and the value of  $p_{\text{O}_2}$  corresponding to the equilibrium (Eq. 9.48) is calculated to be as shown in Fig. 9.39. In a steam cracking reactor, the  $\text{H}_2/\text{H}_2\text{O}$  ratio is approximately unity, and the equilibrium  $p_{\text{O}_2}$  values calculated for



are seen to be much higher than the  $\text{Cr}_3\text{C}_2/\text{Cr}_2\text{O}_3$  values, implying that the oxide is stable. However, as pointed out by Grabke et al. [6], the oxygen activity beneath a

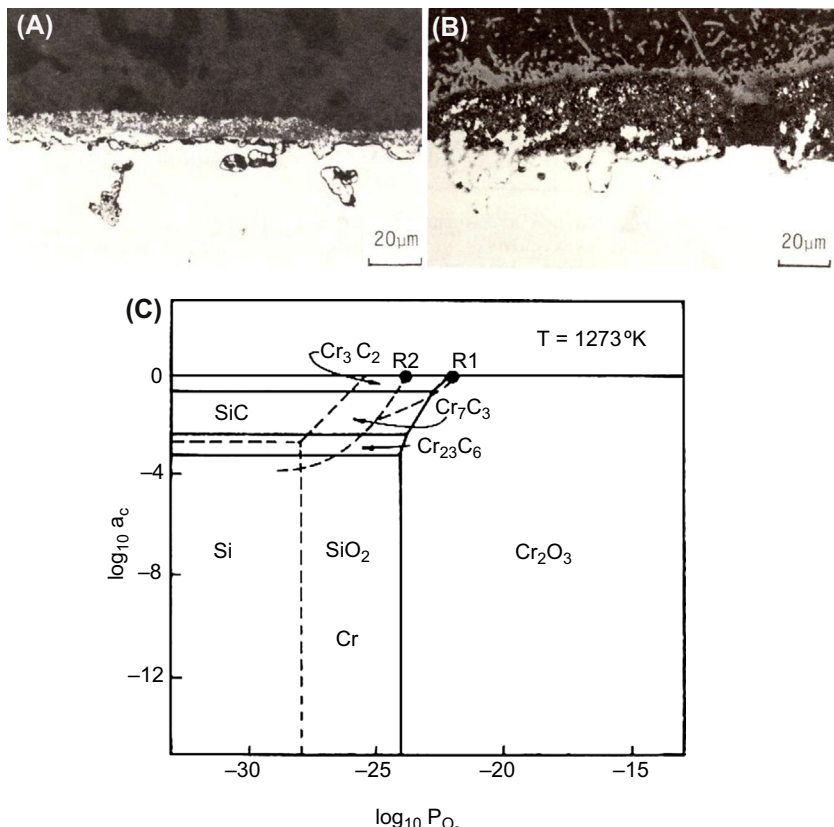


**FIGURE 9.37** Scales grown on 25Cr-35Ni heat-resisting steels at  $1000^\circ\text{C}$  and  $a_{\text{C}} = 1$ : (A)  $p_{\text{O}_2} = 10^{-22}$  atm, (B)  $p_{\text{O}_2} = 10^{-24}$  atm [131] and (C) diffusion paths. With permission from the National Research Council of Canada.

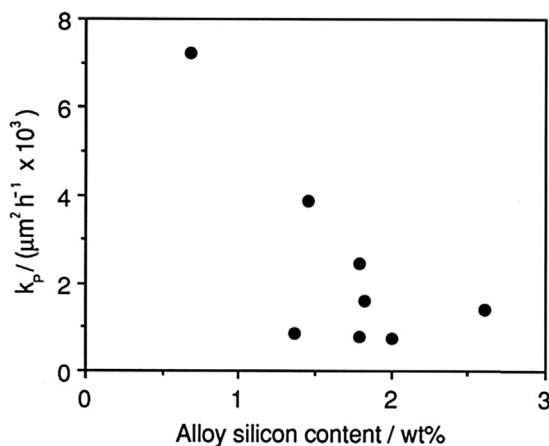


**FIGURE 9.38** Dependence of carburisation rate on alloy silicon content at 1050°C,  $a_C = 1$ ,  $p_{O_2} = 3 \times 10^{-20}$  atm [132]. Published with permission from © NACE International 1982.

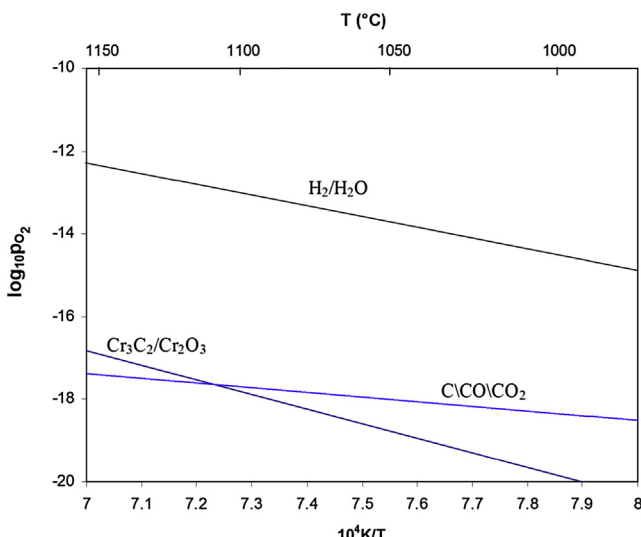


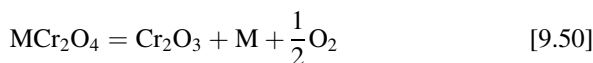
**FIGURE 9.39** Thermodynamics of oxide to carbide conversion compared with CO/CO<sub>2</sub> mixture at  $p_T = 1$  atm in equilibrium with graphite.

carbon deposit can be a great deal less. If the carbon deposit is gas tight, then the gas species will be CO and CO<sub>2</sub>, with the ratio  $p_{CO}^2/p_{CO_2}$  set through the Boussodouard equilibrium (Eq. [9.8]) with unit carbon activity. If the total pressure  $p_{CO} + p_{CO_2} = 1$  atm, the corresponding  $p_{O_2}$  is found from the thermodynamics of Eq. [9.2] to be low at high temperatures (Fig. 9.39). If  $T > 1100^\circ\text{C}$ , carbon will reduce the oxide and degrade the protective nature of the scale.

Both  $\text{Cr}_2\text{O}_3$  and  $\text{Al}_2\text{O}_3$  scales provide effective barriers to carbon entry and metal dusting. However, such scales eventually fail by cracking or spallation. If sufficient chromium or aluminium remains at the alloy surface, then scale rehealing takes place. If not, carbon dissolves in the depleted alloy and diffuses inward, to precipitate carbides. At high carbon activities, metal dusting follows. The competition between outward metal diffusion to form a scale and inward carbon diffusion should, in principle, be described by an equation such as Eq. [9.15]. Unfortunately, no rigorous test of this description is available. Qualitative support is provided by the finding [91] that several heat-resisting alloys could be ranked in their resistance to metal dusting during temperature cycling according to their  $N_{\text{Cr}}^{(0)} D_{\text{Cr}} / N_{\text{C}}^{(s)} D_{\text{C}}$  values.

The failure of oxide scales under creep conditions has been shown [7,133] to lead to accelerated carburisation at high creep rates. However, the strain rates necessary to prevent scale healing are so high [134] that this should not usually be a practical problem.

A practical problem arises in the use of oxide scales for protection against carbon. Preoxidation procedures used to develop a chromia scale prior to service can also develop an outer scale layer of spinel,  $\text{M}\text{Cr}_2\text{O}_4$ . If subsequent service conditions provide an oxygen potential below the spinel stability level, it is reduced, leaving particles of metal,



These particles act as catalytic sites, accelerating the onset of coking. This in turn can lead to scale disintegration and the commencement of dusting. Exposing austenitic chromia-formers to alternately oxidising and carburising conditions has been shown [135] to lead to rapid scale failure, accelerated carburisation and in some cases the commencement of dusting. In order to avoid this effect, it is necessary to adjust the preoxidation conditions so that the oxides formed at that stage are stable during subsequent service.

### 9.8.1 Protection by Adsorbed Sulphur

The introduction of gaseous sulphur species such as  $\text{H}_2\text{S}$  to industrial process steams is widely practiced in order to minimise carburisation and metal dusting. Sulphur adsorbs on the metal surface, preventing carbon access [34,136,137]. Under these conditions, rehealing of damaged oxide scales is favoured over carbon penetration. The effect increases with  $p_{\text{S}_2}$ , but the sulphur pressure must be kept below the value at which  $\text{CrS}$  can form.

Adsorbed sulphur also provides protection against metal dusting, delaying the onset of the process and allowing more time for oxide rehealing to occur. Data assembled by Schneider et al. [138] for the effect on iron are shown in Fig. 9.40. The  $\text{H}_2\text{S}/\text{H}_2$  ratios required to yield protection increase with temperature because

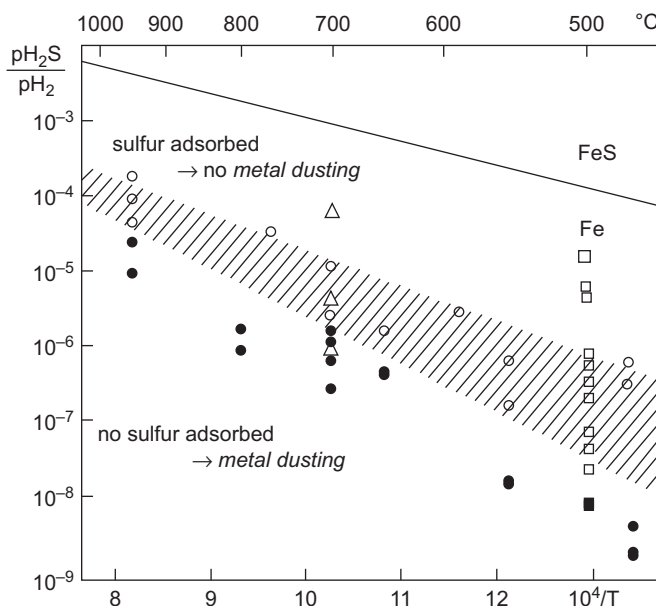


**FIGURE 9.40** Effect of sulphur on metal dusting. The hatched region represents the transition to an iron surface saturated with sulphur [138]. Published with permission from Wiley-VCH.

the sulphur adsorption process is strongly exothermic. In the case of pure iron, the sulphur adsorbs on cementite and prevents the nucleation of graphite.

### 9.8.2 Protection by Coatings

As is by now clear, long-term protection against metal dusting and carburisation can be achieved by forming a stable oxide scale which is capable of rapid rehealing. Coatings with high concentrations of scale-forming elements can be used to provide this protection. Chemical vapour deposition [139–144] and flame spraying [145] have been used to produce carburisation-resistant coatings, and their utility under metal dusting conditions has also been tested [146]. Aluminium diffusion coatings were found to be protective for a series of ferritic metals (2.25–28Cr) and the austenitic alloy 800. However, long-term exposure led to pore development under the scale and cracking. Silicon diffusion coatings did not develop protective scales. A flame-sprayed  $\gamma$ -TiAl coating was successful on a ferritic material but failed on alloy 800 as a result of thermal mismatch. This work showed that alumina scales provided better protection against carbon than did chromia.

Another class of metallic coatings is designed to provide protection against metal dusting by remaining unoxidised and being noncatalytic to carbon deposition. Copper can be used not only as an alloying element (Section 9.7.2), but also in intermetallic coatings [147]. Like copper, tin has very low

solubility for carbon and is noncatalytic to carbon deposition [148]. Tin is not suitable for alloying but forms intermetallics with nickel. Of these,  $\text{Ni}_3\text{Sn}_2$  is suitable as a coating for nickel-base alloys and provides excellent protection against dusting in reducing atmospheres [149,150].

Aguero et al. [151] have summarised the results achieved in resisting metal dusting with a variety of diffusion and overlay coatings.

## 9.9 CONTROLLING CARBON CORROSION

Carburisation reactions at  $a_{\text{C}} \leq 1$  are well-described by the classical theory of internal oxidation. Local equilibrium is achieved within the reacting alloy, solid state diffusion of dissolved carbon controls the rate and parabolic kinetics result. Wagner's diffusion theory provides good quantitative predictive capability, despite the approximate nature of some of its assumptions.

Metal dusting reactions at  $a_{\text{C}} > 1$  proceed according to complex mechanisms which are still not fully defined. Local equilibrium is not achieved within the gas or at the gas–solid interface. It is therefore necessary to consider both the thermodynamic state of the gas and the kinetics of the several parallel gas–solid reactions possible. This requires specification of the complete gas composition, including minority species, as well as temperature. Considerably more work is needed to define temperature and gas composition effects on dusting rates.

Ferritic materials at moderate temperatures form  $\text{Fe}_3\text{C}$ . This phase is either disintegrated by precipitation within it of graphite or, in other gases, decomposed to yield metallic iron. Unfortunately, the boundaries between the two regimes are still not defined. Austenitic materials form no carbide and are disintegrated by precipitation and growth of graphite within the metal. A similar mechanism operates for ferritic materials when cementite formation is prevented by high temperatures or alloying.

Protection against carburisation and dusting requires the provision of a surface barrier between metal and gas, either an adsorbed sulphur layer or an oxide scale. The addition of low levels of sulphur-containing compounds to gas streams is widely practised in the operation of processes such as steam cracking and direct reduction of iron ore. The adventitious presence of sulphur in crude oil provides protection in the early stages of the refining process. However, gaseous sulphur is not always acceptable in process streams, as it can poison catalysts or contaminate the final products.

Steam reforming is a catalysed process in which sulphur is unacceptable, and protection is achieved by providing a barrier oxide scale. Maintaining an effective oxide scale can be difficult under reducing conditions. The chromia-plus-silica scales formed by cast, heat-resistant grades are successful at low carbon activities, but not at the higher activities encountered in cooler gases. In these situations, alumina scales are to be preferred. A variety of proprietary, aluminium-rich coatings is used to form the desired scales. Under some circumstances, FeCrAl alloys such as Kanthal are employed.

When attack by carbon does occur, it is catastrophically rapid. For this reason, protective measures must be employed, and their continued effectiveness monitored.

## REFERENCES

- [1] S.R. Shatynski, *Oxid. Met.* 13 (1978) 105.
- [2] T. Wada, H. Wada, J.F. Elliott, J. Chipman, *Met. Trans.* 3 (1972) 2865.
- [3] T. Wada, H. Wada, J.F. Elliott, J. Chipman, *Met. Trans.* 2A (1971) 2199.
- [4] R.P. Smith, *Acta Met.* 1 (1953) 578.
- [5] H.J. Grabke, E.M. Peterson, *Scripta Met.* 12 (1978) 1111.
- [6] H.J. Grabke, U. Gravenhorst, W. Steinkusch, *Werkst. u. Korros.* 27 (1976) 291.
- [7] A. Schnaas, H.J. Grabke, *Oxid. Met.* 12 (1978) 387.
- [8] G.M. Smith, D.J. Young, D.L. Trimm, *Oxid. Met.* 18 (1982) 229.
- [9] C. Wagner, *Z. Elektrochem.* 63 (1959) 772.
- [10] O. Kubaschewski, C.B. Alcock, P.J. Spencer, *Materials Thermochemistry*, sixth ed., Pergamon, Oxford, 1993.
- [11] F.N. Mazandarany, R.D. Pehlke, *Met. Trans.* 4A (1973) 2070.
- [12] A.T. Allen, D.L. Douglass, *Oxid. Met.* 51 (1999) 199.
- [13] T.A. Ramanarayanan, D.J. Slolovitz, *J. Electrochem. Soc.* 132 (1985) 2268.
- [14] O. Ahmed, D.J. Young, in: M.J. McNallan, E.J. Opila, T. Maruyama, T. Narita (Eds.), *High Temperature Corrosion and Materials Chemistry II*, The Electrochemical Society, Inc., Pennington, N.J., 2000, p. 77.
- [15] R. Benz, J.F. Elliott, J. Chipman, *Met. Trans.* 5 (1974) 2235.
- [16] S. Ford, P.R. Munroe, D.J. Young, *Micron* 32 (2001) 817.
- [17] D.J. Young, O. Ahmed, *Mater. Sci. Forum* 369–372 (2001) 93.
- [18] S. Ford, P.R. Munroe, D.J. Young, in: P.F. Tortorelli, I.G. Wright, P.Y. Hou (Eds.), *John Stringer Symposium*, ASM International, Materials Park OH, 2003, p. 77.
- [19] M. Udyavar, D.J. Young, *Corros. Sci.* 42 (2000) 861.
- [20] S.K. Bose, H.J. Grabke, *Z. Metallk.* 69 (1978) 8.
- [21] S. Ford, D.J. Young, D. McGrouther, P.R. Munroe, *Mater. High Temp.* 22 (2005) 351.
- [22] K.P. Bunin, *Izv. Chern. Metall.* 2 (1973) 123.
- [23] V.I. Mozchan, *Izv. Chern. Metall.* 8 (1979) 92.
- [24] C.H. Toh, P.R. Munroe, D.J. Young, *Oxid. Met.* 58 (2002) 1.
- [25] P. Zsakalos, M. Lundberg, R. Petterson, *Corros. Sci.* 48 (2006) 1679.
- [26] E.K. Ohriner, J.E. Morall, *Scripta Met.* 13 (1979) 7.
- [27] J.S. Kirkaldy, *Canad. Met. Q.* 8 (1969) 35.
- [28] H.-J. Christ, *Mater. Corros.* 49 (1998) 258.
- [29] R.H. Kane, *Corrosion* 37 (1981) 187.
- [30] W.F. Chu, A. Rahmel, *Oxid. Met.* 15 (1981) 331.
- [31] D.B. Roach, I.G. Wright, *The Study of the Carburisation Resistance of Heat Resistant Casting Alloys*, 1st Interim Report on Project No 60, Batelle, Columbus Labs, OH, 1974.
- [32] K. Ledgeff, A. Rahmel, H. Schorr, *Werkst. Korros.* 31 (1980) 121.
- [33] T.A. Ramanarayanan, R. Petkovic-Luton, *Corrosion* 37 (1981) 712.
- [34] J. Barnes, J. Corish, J.F. Norton, *Oxid. Met.* 26 (1986) 333.
- [35] S.P. Kinniard, D.J. Young, D.L. Trimm, *Oxid. Met.* 26 (1986) 417.
- [36] D.R.G. Mitchell, D.J. Young, *Foundry Trade J.* 166 (1992) 253.

- [37] D.R.G. Mitchell, D.J. Young, *J. Mat. Sci. Lett.* 12 (1993) 1076.
- [38] D.R.G. Mitchell, D.J. Young, W. Kleeman, *Mater. Corros.* 49 (1998) 231.
- [39] P. Becker, F. Ouamara, D.J. Young, in: E. Opila, P. Hou, T. Moruyama, B. Pieraggi, D. Schifler, E. Wachina (Eds.), *High Temperature Corrosion Materials Chemistry IV*, The Electrochemical Society, Inc., Pennington, NJ, 2003, p. 178.
- [40] P. Becker, D.J. Young, *Oxid. Met.* 67 (2007) 267.
- [41] J. Klower, U. Heubner, *Mater. Corros.* 49 (1998) 237.
- [42] J.F. Norton, L. Blidegn, S. Canetoli, P.D. Frampton, *Werkst. Korros.* 32 (1981) 467.
- [43] S. Forseth, P. Kofstad, *Mater. Corros.* 49 (1998) 266.
- [44] H.J. Grabke, *Carburisation – A High Temperature Corrosion Phenomenon*, MTI Publication No. 52, Materials Technology Institute of the Chemical Processing Industries, St. Louis, MI, 1997.
- [45] H. Lewis, *B. Corros. J.* 3 (1968) 166.
- [46] H.J. Grabke, I. Wolf, *Mater. Sci. Eng.* 87 (1987) 23.
- [47] A. Rahmel, H.J. Grabke, W. Steinkusch, *Mater. Corros.* 49 (1998) 221.
- [48] S.K. Roy, H.J. Grabke, W. Wepner, *Arch. Eisenhuttenwes.* 51 (1980) 91.
- [49] J. Hemptenmacher, H.J. Grabke, *Werkst. Korros.* 34 (1983) 333.
- [50] E. Camp, C. Phillips, L. Cross, *Corrosion* 10 (1954) 149.
- [51] W.G. Hubbell, *The Iron Age* 157 (1946) 56.
- [52] O.L. Burns, *Corrosion* 6 (1950) 169.
- [53] P.A. Lefrancois, W.B. Hoyt, *Corrosion* 19 (1963) 360t.
- [54] R.F. Hochman, in: Proc. 3rd Int. Cong. Met. Corrosion, University of Moscow Press, 1969.
- [55] R.F. Hochman, M.G. Klett, in: Proc. 5th Int. Cong. Met. Corrosion, NACE, Houston, TX, 1974.
- [56] R.F. Hochman, in: Z.A. Foroulis, F.S. Pettit (Eds.), *Proc. Symp. Properties of High Temperature Alloys with Emphasis on Environmental Effects*, Electrochemical Society, Pennington, NJ, 1977, p. 571.
- [57] H.J. Grabke, J. Hemptenmacher, A. Munker, *Werkst. Korros.* 35 (1984) 543.
- [58] J.C. Nava Paz, H.J. Grabke, *Oxid. Met.* 39 (1993) 437.
- [59] H.J. Grabke, R. Krajak, J.C. Nava Paz, *Corros. Sci.* 35 (1993) 1141.
- [60] H.J. Grabke, R. Krajak, E.M. Muller-Lorenz, *Werkst. Korros.* 44 (1993) 89.
- [61] H.J. Grabke, C.B. Bracho-Troconis, E.M. Muller-Lorenz, *Werkst. Korros.* 45 (1994) 215.
- [62] M.A.A. Motin, P.R. Munroe, M.P. Brady, D.J. Young, *Scripta Mater.* 56 (2007) 281.
- [63] E. Pippel, J. Woltersdorf, H.J. Grabke, S. Strauss, *Steel Res.* 66 (1995) 217.
- [64] E. Pippel, J. Woltersdorf, R. Schneider, *Mater. Corros.* 49 (1998) 309.
- [65] C.M. Chun, J.D. Mumford, T.A. Ramanarayanan, *J. Electrochem. Soc.* 149 (2002) B348.
- [66] B. Schmid, J.C. Walmsley, O. Grong, R. Odegard, *Met. Mat. Trans. A.* 34A (2003) 345.
- [67] Z. Zeng, K. Natesan, V.A. Maroni, *Oxid. Met.* 58 (2002) 147.
- [68] J. Zhang, A. Schneider, G. Inden, *Corros. Sci.* 45 (2003) 1329.
- [69] J. Zhang, A. Schneider, G. Inden, *Corros. Sci.* 45 (2003) 281.
- [70] J. Zhang, A. Schneider, G. Inden, *Mater. Corros.* 54 (2003) 770.
- [71] C.H. Toh, P.R. Munroe, D.J. Young, *Mater. High Temp.* 20 (2003) 527.
- [72] R.T.K. Baker, M.A. Barber, P.S. Harris, F.S. Yeates, R.J. Waite, *J. Catal.* 26 (1972) 51.
- [73] R.J. Longbottom, O. Ostrovski, J. Zhang, D.J. Young, *Met. Mat. Trans. B.* 38 (2007) 175.
- [74] R.P. Smith, *Trans. AIME* 224 (1962) 105.
- [75] E.T. Turkdogan, *Physical Chemistry of High Temperature Technology*, Academic Press, New York, 1980.

- [76] I. Koszman, in: S.A. Jansson, Z.A. Fououlis (Eds.), *Proc. Symp. On High Temp. Gas-Metal Reactions in Mixed Environments*, Met. Soc. AIME, New York, 1973, p. 155.
- [77] B. Ozturk, V.L. Fearing, J.A. Ruth, G. Simkovich, *Met. Trans. A* 13A (1982) 1871.
- [78] A. Schneider, G. Inden, *Calphad* 31 (2007) 141.
- [79] M.A.A. Motin, J. Zhang, D.J. Young, *J. Electrochem. Soc.* 157 (2010) C375.
- [80] P. Szakalos, *Mater. Corros.* 54 (2003) 752.
- [81] J. Zhang, A. Schneider, G. Inden, *Mater. Corros.* 54 (2003) 763.
- [82] H.J. Grabke, *Mater. Corros.* 54 (2003) 736.
- [83] C.M. Chun, T.A. Ramanarayanan, *Oxid. Met.* 62 (2004) 71.
- [84] E.M. Muller-Lorenz, H.J. Grabke, *Mater. Corros.* 50 (1999) 614.
- [85] H. Yin, J. Zhang, D.J. Young, *Corros. Sci.* 51 (2009) 2983.
- [86] A. Schneider, H. Vielhaus, G. Inden, H.J. Grabke, E.M. Muller-Lorenz, *Mater. Corros.* 49 (1998) 336.
- [87] H.J. Grabke, *Corrosion* 51 (1995) 711.
- [88] H.J. Grabke, E.M. Muller-Lorenz, B. Eltester, M. Lucas, D. Monceau, *Steel Res.* 68 (1997) 179.
- [89] A.S. Frabiezwski, W.R. Watkins, J.J. Hoffman, S.W. Dean, *Corrosion 2000*, NACE, Houston, TX, 2000 paper no. 532.
- [90] B.A. Baker, G.D. Smith, *Corrosion 2000*, NACE, Houston, TX, 2000 paper no. 257.
- [91] C.H. Toh, P.R. Munroe, D.J. Young, K. Fogar, *Mater. High Temp.* 20 (2003) 129.
- [92] H.J. Grabke, *Mater. Corros.* 49 (1998) 303.
- [93] S. Strauss, R. Krajak, M. Palm, H.J. Grabke, *Mater. Corros.* 47 (1996) 701.
- [94] A. Schneider, J. Zhang, *Mater. Corros.* 54 (2003) 778.
- [95] A. Schneider, J. Zhang, *J. Corros. Sci. Eng.* 6 (2003) paper H043.
- [96] R. Schneider, E. Pippel, J. Woltersdorf, S. Strauss, H.J. Grabke, *Steel Res.* 68 (1997) 326.
- [97] J. Zhang, D.J. Young, *Corros. Sci.* 49 (2007) 1496.
- [98] C.M. Chun, J.D. Mumford, T.A. Ramanarayanan, *J. Electrochem Soc.* 147 (2000) 3680.
- [99] Z. Zeng, K. Natesan, *Chem. Mater.* 15 (2003) 872.
- [100] Q. Wei, E. Pippel, J. Woltersdorf, S. Strauss, H.J. Grabke, *Mater. Corros.* 51 (2000) 652.
- [101] J. Zhang, D.J. Young, *Acta Mater.* 56 (2008) 68.
- [102] E. Pippel, J. Woltersdorf, H.J. Grabke, *Mater. Corros.* 54 (2003) 747.
- [103] J.C. Shelton, H.R. Patil, J.M. Blakely, *Surf. Sci.* 43 (1974) 493.
- [104] R.T. Yang, J.P. Chen, *J. Catal.* 115 (1989) 52.
- [105] J. Zhang, D.M.I. Cole, D.J. Young, *Mater. Corros.* 56 (2005) 756.
- [106] H.J. Grabke, R. Krajak, E.M. Muller-Lorenz, S. Strauss, *Mater. Corros.* 47 (1996) 495.
- [107] J. Zhang, D.J. Young, *Corros. Sci.* 56 (2012) 184.
- [108] D.J. Young, M.A.A. Motin, J. Zhang, *Defects Diffus. Forum* 289–292 (2009) 51.
- [109] Y. Nishiyama, N. Otsuka, *Mater. Sci. Forum* 522–523 (2006) 581.
- [110] C.A. Bernardo, I. Alstrup, J.R. Rostrup-Nielsen, *J. Catal.* 96 (1985) 517.
- [111] I. Alstrup, M.T. Tavares, C.A. Bernardo, O. Sorensen, J.R. Rostrup-Nielsen, *Mater. Corros.* 49 (1998) 367.
- [112] M.T. Tavares, I. Alstrup, C.A. Bernardo, *Mater. Corros.* 50 (1999) 681.
- [113] J.A. Dalmon, G.A. Martin, *J. Catal.* 49 (1998) 367.
- [114] DKI German Copper Institute Booklet: Copper Nickel Alloys: Properties, Processing, Application. [http://www.copper.org/applications/cuni/txt\\_DKI.html](http://www.copper.org/applications/cuni/txt_DKI.html).
- [115] R.B. Mclellan, P. Chraska, *Mater. Sci. Eng.* 6 (1970) 176.
- [116] J. Zhang, M. Safarzadeh, D.J. Young, *Oxid. Met.* 70 (2008) 15.
- [117] Y. Nishiyama, K. Moriguchi, N. Otsuka, T. Kudo, *Mater. Corros.* 56 (2005) 806.

- [118] H.J. Grabke, E.M. Muller-Lorenz, J. Klower, D.C. Agarwal, Mater. Perform. 37 (1998) 58.
- [119] M. Maier, J.F. Norton, P. Puschek, Mater. High Temp. 17 (2000) 347.
- [120] R.A. Perkins, W.C. Coons, F.J. Radd, in: Z.A. Farouli, F.S. Pettit (Eds.), Properties of High Temperature Alloys, Electrochemical Society, Inc., Princeton, NJ, 1976, p. 733.
- [121] M. Maier, J.F. Norton, Corrosion 99, NACE, Houston, TX, 1999 paper 75.
- [122] Z. Zeng, K. Natesan, M. Grimoditch, Corrosion 60 (2004) 632.
- [123] S. Strauss, H.J. Grabke, Mater. Corros. 49 (1998) 321.
- [124] J. Litz, A. Rahmel, M. Schorr, Oxid. Met. 29 (1988) 95.
- [125] J. Zhang, D.J. Young, Corros. Sci. 49 (2007) 1450.
- [126] P. Szakalos, R. Pettersson, S. Hertzman, Corros. Sci. 44 (2002) 2253.
- [127] W. Betteridge, The Nimonic Alloys, E. Arnold, London, 1959.
- [128] I. Wolf, H.J. Grabke, Solid State Commun. 54 (1985) 5.
- [129] H.J. Grabke, K. Ohla, J. Peters, I. Wolf, Werkst. Korros. 34 (1983) 495.
- [130] X.G. Zheng, D.J. Young, Oxid. Met. 42 (1994) 163.
- [131] P. Tomas, D.J. Young, D.L. Trimm, in: Proc. Int. Congress Met. Corros, vol. 1, National Research Council of Canada, Ottawa, 1984, p. 58.
- [132] D.R.G. Mitchell, D.J. Young, W. Kleeman, Corrosion 92, NACE, Houston, TX, 1992 paper 302.
- [133] L. Dillinger, R.D. Buchheit, J.A. Van Echo, D.B. Roach, A.M. Hall, Microstructures of Heat-resistant-alloys, Steel Founders' Society of America, Rocky River, OH, 1970.
- [134] M. Schutze, Oxid. Met. 25 (1986) 409.
- [135] M.A. Harper, M. Ducasse, D.J. Young, Corrosion 51 (1995) 191.
- [136] H.J. Grabke, E.M. Peterson, S.R. Srinivasan, Surf. Sci. 67 (1977) 501.
- [137] H.J. Grabke, R. Moller, A. Schnaas, Werkst. Korros. 30 (1979) 794.
- [138] A. Schneider, H. Viefhaus, G. Inden, H.J. Grabke, E.M. Muller-Lorenz, Mater. Corros. 49 (1998) 336.
- [139] G. Southwell, S. MacAlpine, D.J. Young, J. Mater. Sci. Eng. 88 (1987) 81.
- [140] B. Ganser, K.A. Wynns, A. Kurlekar, Mater. Corros. 50 (1999) 700.
- [141] R.A. Rapp, Corrosion 89, NACE, Houston, TX, 1989 paper 532.
- [142] R. Streiff, in: N.B. Dahotre, J.M. Hampikian (Eds.), Elevated Temperature Coatings: Science and Technology II, TMS, 1996, p. 407.
- [143] R.L. Wachtell, in: B.N. Chapman, J.C. Anderson (Eds.), Science and Technology of Surface Coating, Academic Press, London, 1974, p. 105.
- [144] S.C. Kung, R.A. Rapp, Oxid. Met. 32 (1989) 89.
- [145] M. Schutze, Ger. Patent: DE 197 43 421.5 (1998).
- [146] C. Rozado, M. Schutze, Mater. Corros. 54 (2003) 831.
- [147] T.A. Ramanarayanan, C.M. Chun, J.D. Mumford, US Pat. 6,737,175 (2004).
- [148] E. Nikolla, A. Holewinski, J. Schwank, S. Linic, J. Amer. Chem. Soc. 128 (2006) 11354.
- [149] C. Geers, M. Galetz, M. Schütze, Surf. Coat. Technol. 215 (2013) 2.
- [150] D.J. Young, J. Zhang, C. Geers, M. Schütze, Mater. Corros. 61 (2011) 7.
- [151] A. Agüero, M. Gutiérrez, L. Korcakova, T.T.M. Nguyen, B. Hinemann, S. Saadi, Oxid. Met. 76 (2011) 23.